

Numerically generated axisymmetric black hole spacetimes: Numerical methods and code tests

David Bernstein,^{1,2,*} David Hobill,^{1,3} Edward Seidel,^{1,2} Larry Smarr,^{1,2} and John Towns¹

¹ *National Center for Supercomputing Applications, 605 E. Springfield Avenue, Champaign, Illinois 61820*

² *Department of Physics, University of Illinois, Urbana, Illinois 61801*

³ *Department of Physics and Astronomy, University of Calgary, Calgary, Alberta, Canada T2N 1N4*

(Received 7 March 1994; revised manuscript received 12 July 1994)

We develop a flexible computer code to study axisymmetric black hole spacetimes. The code is currently set up to evolve the fully nonlinear Einstein equations in azimuthal and equatorial plane symmetry. The initial data for this code generally consists of a combination of one black hole and an arbitrary amplitude, time symmetric gravitational wave. We present a discussion of the mathematical framework for the problem, various coordinate and time slice choices, and a battery of code tests.

PACS number(s): 04.25.Dm, 04.30.Db, 95.30.Sf, 97.60.Lf

I. INTRODUCTION

A. Overview

In this paper we report on a computer code developed to study the fully nonlinear Einstein equations for axisymmetric spacetimes. This code represents an essential step in a longer term program to develop codes for solving the Einstein equations in the absence of any symmetries. The motivation for such a project is severalfold. (1) Such codes will be required to perform calculations of fully relativistic sources of gravitational waves. Calculations of this nature will be important for a theoretical understanding of gravitational wave astronomy, which promises to provide a new window on the astrophysical Universe [1]. Currently there exist no analytic techniques for computing waveforms expected from promising sources of strong gravitational waves, such as the coalescence of rotating black holes. Computational methods are currently our only recourse for computing such waveforms. (2) The study of general relativity itself as a fundamental theory of physics is a difficult undertaking, due in part to the complicated, nonlinear nature of the equations. Of all the analytic solutions found in the past 75 years of study only a relatively small number correspond to astrophysically interesting situations and these are usually very idealized, e.g., the Schwarzschild and Kerr solutions. The study of these solutions and their perturbations has been extremely fruitful, helping to shape our understanding of the theory as a whole. However, not being strongly dynamical, they represent only a small part of the "solution space" of general relativity. The study of the strongly dynamical regions should provide new insights into the nature of the Einstein equations. (3) In

the past decade the power of the fastest single processor vector computers has increased by perhaps an order of magnitude, while the next 5 years should witness an increase of 1000 times in overall power due to the development of massively parallel machines. If the current state of numerical relativity is used as a guide, this acceleration in the power of supercomputers should make possible the computation of complex, strongly dynamical, astrophysically realistic spacetimes. It is hoped that the study of the Einstein equations, a complicated set of hyperbolic and elliptic equations, can act as a driving force to develop accurate numerical techniques suitable for this new generation of machines.

In this paper we discuss a suite of codes which has been developed at NCSA over the past 5 years. The codes are specialized for the computation of axisymmetric, equatorial plane symmetric spacetimes and have been applied to systems consisting of a single oscillating black-hole and the head-on collision of two equal mass black holes. Overall the metric, numerical methods, and spacetime analysis tools used to compute and analyze the data for these two systems are exactly the same. Where the codes differ is in the boundary conditions, initial conditions, and the computational grid used to match the geometry of the different topologies. Here we will refer to this suite of codes as "the code" with the understanding that the results obtained by one code are not significantly different from those obtained by the other codes. (A modified version of this code has been used to evolve the collision of two equal mass black holes, as described in Ref. [2].) The emphasis in this paper is on the numerical algorithms used and various tests of the code's accuracy, convergence, and stability. Companion papers [3,4] are devoted to other aspects of this system. In [3,5,6], we discuss many details of the initial-value problem for this system, which consists of a time symmetric gravitational wave superimposed on a black hole. For completeness, some details of the distorted black hole initial data are provided in Secs. IIC and IID, but a full discussion appears in Refs. [3,5]. In another paper [4] we discuss the evolution of low and moderate amplitude gravitational

*Present address: Department of Mathematics, Statistics and Computing Science, University of New England, Armidale, NSW 2351, Australia.

waves in the black hole spacetime. An overview of the project, details of the numerical code, and a complete version of the code itself are being published in [7].

The paper is organized as follows. In Sec. II we describe the mathematical framework of the calculation, including a brief review of the 3+1 formalism used to evolve the Einstein equations, the metric form we use, boundary conditions, and choices of time slicing and spatial gauges. In Sec. III we discuss the numerical algorithms we use for both the hyperbolic and elliptic equations in the system. In Sec. IV we present a series of code tests, including stability and convergence tests, and comparison with a carefully tested code which computes the solution assuming spherical symmetry. In Sec. V we summarize and outline future work planned for this code.

II. MATHEMATICAL DEVELOPMENT

In this section we describe the mathematical framework for the calculation of our black hole spacetimes, including a brief summary of the 3+1 formulation of general relativity, the specialization of this formalism to our axisymmetric system, the boundary conditions provided by the symmetries in our system, a discussion of the initial value problem, and coordinate conditions used in our code.

A. The 3+1 formalism

The 3+1 [or Arnowitt-Deser-Misner (ADM)] formalism of general relativity is a common starting point for many numerical relativity calculations. The formalism is reviewed in many places [8] and we refer the interested reader to those references. In this section the essential features of the formalism are summarized. We use geometrized units, in which Newton's constant G , and the speed of light c , are equal to unity. Greek indices will run from 0 to 3, latin indices from 1 to 3.

The central idea is to view spacetime as a foliation of three-dimensional spatial hypersurfaces, called slices, each labeled with a unique value of a parameter t , which may be identified as a time coordinate. Each hypersurface inherits a positive definite three-metric from the surrounding spacetime and is endowed with an extrinsic curvature tensor K_{ab} , which describes the expansion of the unit normal vector field to the slice. The full spacetime metric is written in the ADM form [9]

$$ds^2 = -(\alpha^2 - \beta_a \beta^a) dt^2 + 2\beta_a dx^a dt + \gamma_{ab} dx^a dx^b, \quad (1)$$

where the lapse function α determines the foliation and the shift vector β^a determines how the slices are threaded by the spatial coordinates. These functions essentially determine the spacetime coordinate system and thus can be chosen freely. Various choices used in our code are discussed in Secs. IIE2 and IIE3.

As with any other tensor, the Ricci tensor of the spacetime may be decomposed into its spatial and timelike components, and when the vacuum Einstein equation is

imposed these reduce to the four constraint equations

$$R + (\text{tr}K)^2 - K^{ab}K_{ab} = 0, \quad (2)$$

$$D_b(K^{ab} - \gamma^{ab}\text{tr}K) = 0, \quad (3)$$

and the 12 evolution equations

$$\partial_t \gamma_{ab} = -2\alpha K_{ab} + D_a \beta_b + D_b \beta_a, \quad (4)$$

$$\begin{aligned} \partial_t K_{ab} = & -D_a D_b \alpha + \alpha [R_{ab} + (\text{tr}K)K_{ab} - 2K_{ac}K^c_b] \\ & + \beta^c D_c K_{ab} + K_{ac} D_b \beta^c + K_{cb} D_a \beta^c. \end{aligned} \quad (5)$$

Here R_{ab} is the Ricci tensor, R the scalar curvature, and D_a the covariant derivative associated with γ_{ab} . The Einstein equations are contained in (2), (3), and (5), while Eq. (4) follows from the definition of the extrinsic curvature. In our work the initial-value problem is time symmetric and the Hamiltonian constraint is solved on an "initial" hypersurface using the well-known conformal decomposition method developed by Lichnerowicz [10], studied by Brill [11], and Misner [12] in special cases and described in detail by York [8]. The initial data is then evolved forward in time using the evolution equations (4) and (5).

If the constraints are satisfied on any hypersurface the Bianchi identities guarantee that they remain satisfied on all subsequent hypersurfaces. In a numerical solution, this may not be the case and the constraints have to be monitored carefully in order to ensure that the spacetimes generated are accurate. Traditional alternatives to this approach involve solving the constraint equations on each slice for certain metric and extrinsic curvature components, and then simply monitoring the "leftover" evolution equations. This issue is discussed further in this paper in Sec. IV, by Choptuik in Ref. [13], and in more detail for the Schwarzschild spacetime in Ref. [14]. New approaches to this problem of constraint vs evolution equations are currently being pursued [15,16].

B. Form of the metric

In general relativity it is common practice to assume a special form for the metric components in terms of other functions of the spacetime coordinates in order to facilitate or simplify calculations within the theory. In numerical relativity, where one is attempting to find general solutions with few or no spacetime symmetries, lengthy calculations are difficult to avoid no matter how one writes the metric. Here we choose to write the spacetime metric in a general form so that a number of special gauge choices can be tested easily. For a nonrotating, axisymmetric spacetime one may write the three-metric in the most general form in spherical polar coordinates as

$$dl^2 = \tilde{A} dr^2 + 2\tilde{C} r dr d\theta + \tilde{B} r^2 d\theta^2 + \tilde{D} r^2 \sin^2 \theta d\phi^2, \quad (6)$$

where \tilde{A} , \tilde{B} , \tilde{C} , and \tilde{D} are functions of r , θ , and t . The metric functions $\gamma_{\theta\phi}$ and $\gamma_{r\phi}$ must vanish because a nonrotating axisymmetric metric must not change under the

operation $\phi \rightarrow -\phi$. For numerical reasons (discussed below) we introduce the coordinate η by

$$r = \frac{m}{2} e^\eta, \quad (7)$$

where m is a general length scaling parameter and r is an “isotropic” radial coordinate. In the (η, θ, ϕ) coordinates the spatial line element becomes

$$dl^2 = \frac{m^2}{4} e^{2\eta} (Ad\eta^2 + 2Cd\eta d\theta + Bd\theta^2 + D \sin^2\theta d\phi^2). \quad (8)$$

In solving the initial-value problem we use the conformal decomposition method mentioned above and we have chosen to leave the three-metric in conformal form for the entire calculation, giving it the final form

$$dl^2 = \Psi^4 (Ad\eta^2 + 2Cd\eta d\theta + Bd\theta^2 + D \sin^2\theta d\phi^2) \quad (9)$$

(the factor $e^{2\eta}m^2/4$ has been absorbed into Ψ).

The full spacetime metric thus appears as

$$g_{\mu\nu} = \begin{pmatrix} -\alpha^2 + \beta^i\beta_i & \beta_\eta & \beta_\theta & 0 \\ \beta_\eta & A & C & 0 \\ \beta_\theta & C & B & 0 \\ 0 & 0 & 0 & D \sin^2\theta \end{pmatrix} \Psi^4. \quad (10)$$

For numerical reasons we have chosen to write the extrinsic curvature tensor K_{ab} in similar conformal form

$$K_{ab} = \Psi^4 \begin{pmatrix} H_A & H_C & 0 \\ H_C & H_B & 0 \\ 0 & 0 & H_D \sin^2\theta \end{pmatrix}. \quad (11)$$

This choice simplifies the evolution equations slightly. (It is, however, not the standard form used in the York method. Fortunately this is unimportant since we are not solving the momentum constraint.)

This leaves us with eight dynamical variables A , B , C , D , H_A , H_B , H_C , and H_D and three gauge quantities α , β^η , and β^θ . The conformal factor Ψ is chosen to be time independent. It could be absorbed into the initial data for the three-metric γ_{ab} , and then it would not appear in the evolution equations. However we have chosen not to do this, evolving the conformal three-metric and extrinsic curvature components instead. Because of our use of the η coordinate, the spatial interval between radial grid points gets quite large at large radii, and this is reflected in steeply increasing metric components far from the black hole. All of this information is encoded into the conformal factor Ψ , leaving the conformal metric functions A , B , and D to approach unity far from the hole. We have found the numerical solution to be better behaved if we evolve functions that asymptotically approach unity, such as A , B , and D , instead of evolving the full three-metric variables that have the conformal factor Ψ absorbed into them.

For our problem the Einstein equations are broken into 11 equations for the 8 dynamical variables; 8 evolution equations and 3 constraint equations. In this work the

constraints will be solved only on the initial slice, after which the evolution equations alone will be used to compute the solution. The three gauge quantities (i.e., the lapse and the two shift vector components) will usually be determined from two elliptic equations (Secs. IIE 2 and IIE 3).

C. Boundary conditions

For practical reasons we have given the spacetimes equatorial plane symmetry as well as axisymmetry, hence the region $\pi/2 \leq \theta \leq \pi$ is identical to the region $0 \leq \theta \leq \pi/2$. (The details of this section apply mainly to the black hole plus gravitational wave spacetimes. The boundary conditions for the two black hole spacetimes are very similar, but not identical, and will be discussed in Ref. [2].) As discussed in detail in Ref. [3], we have used the Einstein-Rosen bridge construction to form a black hole from pure geometry, as in the textbook Schwarzschild solution, but it has been generalized to a nonspherical, nonconformally flat black hole. However, the Einstein-Rosen bridge topology still allows the use of an isometry which maps the metric exterior to the isometry surface onto the interior, providing boundary conditions for the metric components at the isometry surface. The boundaries of the computational grid are, therefore, the axis of symmetry ($\theta = 0$), the equator ($\theta = \pi/2$), an “outer” boundary in the asymptotically flat region of the spacetime, and the isometry surface. The isometry surface may be chosen to lie on a constant radial coordinate surface which we have designated as $\eta = 0$.

On the axis, equator, and isometry surfaces, boundary conditions for the three-metric and extrinsic curvature components can be determined from symmetry conditions. As an example consider the boundary condition at the throat. Here we assume that the region $\eta < 0$ is isometric to the region $\eta > 0$ and hence that there is a transformation $\eta'(\eta, \theta)$ and $\theta'(\eta, \theta)$ which preserves the form of the three-metric, where η' is the radial coordinate in the region $\eta < 0$. If we assume a form for this transformation then boundary conditions at the throat on the three-metric components will result. The simplest such transformation is $\eta' = -\eta$, $\theta' = \theta$ and this combined with the usual tensor transformation rule and continuity of the first derivative gives (e.g., for γ_{11})

$$\left. \frac{\partial \gamma_{11}}{\partial \eta} \right|_{\eta=0} = 0. \quad (12)$$

Since $\gamma_{11} = \Psi^4 A$ we may evidently choose the boundary conditions for Ψ and A independently as long as they satisfy (12). We have chosen the simplest possible conditions whereby Ψ is symmetric through the throat (as in the Schwarzschild solution) and this requires A to be symmetric through the throat as well. It can easily be seen that the components B and D are also symmetric, while the off-diagonal component C is antisymmetric.

The same reasoning can also be used at the axis and equator (due to axisymmetry and equatorial plane sym-

metry $\theta \rightarrow -\theta$ and $\phi \rightarrow \pi - \phi$ are also isometry operations) and thus the boundary conditions on all three surfaces for the metric components are

$$\partial_\theta \Psi|_{\theta=0} = \partial_\theta \Psi|_{\theta=\pi/2} = \partial_\eta \Psi|_{\eta=0} = 0, \quad (13)$$

$$\partial_\theta A|_{\theta=0} = \partial_\theta A|_{\theta=\pi/2} = \partial_\eta A|_{\eta=0} = 0, \quad (14)$$

$$\partial_\theta B|_{\theta=0} = \partial_\theta B|_{\theta=\pi/2} = \partial_\eta B|_{\eta=0} = 0, \quad (15)$$

$$\partial_\theta D|_{\theta=0} = \partial_\theta D|_{\theta=\pi/2} = \partial_\eta D|_{\eta=0} = 0, \quad (16)$$

$$C|_{\theta=0} = C|_{\theta=\pi/2} = C|_{\eta=0} = 0. \quad (17)$$

The symmetry of the extrinsic curvature is not completely determined by the isometry of the upper and lower sheets; one can choose the ‘‘isometry sign’’ of the extrinsic curvature (note that the constraint equations do not determine the isometry sign of K_{ab} , see [17]). However an inspection of the evolution equations, specifically (4), shows that the lapse function must have the same isometry sign. For example, if one specifies that K_{11} be antisymmetric through the isometry surface then so must the lapse function. Requiring the lapse to be antisymmetric through the isometry surface will prevent any evolution of the three-metric there (in the absence of a shift vector). This choice has been made in the study of two colliding black holes [2,18,19]. Here we have chosen a positive isometry sign for the extrinsic curvature. This choice, together with the conditions above, gives the conformal components of K_{ab} the same symmetry behavior as their three-metric counterparts:

$$\partial_\theta H_A|_{\theta=0} = \partial_\theta H_A|_{\theta=\pi/2} = \partial_\eta H_A|_{\eta=0} = 0, \quad (18)$$

$$\partial_\theta H_B|_{\theta=0} = \partial_\theta H_B|_{\theta=\pi/2} = \partial_\eta H_B|_{\eta=0} = 0, \quad (19)$$

$$\partial_\theta H_D|_{\theta=0} = \partial_\theta H_D|_{\theta=\pi/2} = \partial_\eta H_D|_{\eta=0} = 0, \quad (20)$$

$$H_C|_{\theta=0} = H_C|_{\theta=\pi/2} = H_C|_{\eta=0} = 0. \quad (21)$$

These imply

$$\partial_\theta \alpha|_{\theta=0} = \partial_\theta \alpha|_{\theta=\pi/2} = \partial_\eta \alpha|_{\eta=0} = 0. \quad (22)$$

Note that, because of the simplicity of the isometry transformation, not only are the two sheets isometric but also that their respective metrics are written in the same form. Hence the components of γ_{ab} and K_{ab} are *identical* functions of η and θ on all eight patches of the Einstein-Rosen bridge (up to sign for the off diagonal components). This naturally leads to boundary conditions on the components of the shift. The radial component β^η is antisymmetric across the throat guaranteeing that it vanish there, preserving the coordinate position

of the isometry surface. Similarly β^θ is antisymmetric across $\theta = 0$ and $\pi/2$ preserving the coordinate position of the axis of symmetry and the equatorial plane. Hence

$$\beta^\theta|_{\theta=0} = \beta^\theta|_{\theta=\pi/2} = \beta^\eta|_{\eta=0} = 0. \quad (23)$$

It can also be seen that

$$\partial_\theta \beta^\eta|_{\theta=0} = \partial_\theta \beta^\eta|_{\theta=\pi/2} = \partial_\eta \beta^\theta|_{\eta=0} = 0. \quad (24)$$

At the outer boundary one would like to have an outgoing wave condition, assuming the boundary is placed far enough away from the source that an insignificant amount of radiation is expected to be incoming there (e.g., from backscatter off of the background curvature). In this work we have usually chosen the outer boundary of the grid to be further from the isometry surface than radiation propagating off the initial slice could reach at the time the code is stopped. However, the spatial coordinates we use can cause the waves to backscatter off the grid well before they approach the outer boundary (see Sec. II E 1). As discussed in [4] this effect can be reduced by running the code with a larger number of radial zones.

Because of this situation the outer boundary condition has not proved crucial. We have used two types of outer boundary conditions, ‘‘static’’ and ‘‘outgoing.’’ For both types one finite differences the metric and extrinsic curvature components at the grid edge in the usual way by using a set value for the variable one zone off the edge of the grid. In the static condition these values are unity for A , B , and D , and zero for C and all of the extrinsic curvature components. For the outgoing condition these values are updated according to the scheme

$${}^b A^{n+1}_j = A^n_j, \quad (25)$$

where ${}^b A^{n+1}_j$ is the value of the variable A located radially one $\Delta\eta$ from the grid edge and at angular grid point j to be used on time step $n + 1$. We therefore take the value of A on the grid edge at time step n and use this in forming the spatial derivative of A at the grid edge on the next time step. To account for the wave propagation on a curved spacetime background we have also experimented with an outgoing wave boundary condition which should allow us to move the outer boundary in significantly. This will be discussed in a future paper.

1. 2 black hole collisions

An extensively modified version of this code has also been used to study the collision of 2 black holes [2,19,20]. The initial data set of Misner [12] for two time symmetric, axisymmetric Einstein-Rosen bridges connecting two identical asymptotically flat spacetimes can be written directly in our coordinate gauge. Unfortunately, the usual spherical-polar and cylindrical (ρ, z) coordinate systems are not ideally suited to the symmetries present in the two black hole system, so a coordinate system devised by Cadez [21,22] to match the surfaces of black holes and to be spherical far from the holes can be introduced. We

have been able to evolve the collision and to extract the normal mode oscillations of the final black hole, but these calculations are considerably more difficult than the distorted black hole calculations. Full details of the colliding black hole system are presented in Ref. [2].

D. Initial data

The initial data for the black hole plus gravitational wave spacetime are described extensively in Refs. [3,5] where many of its properties are discussed. In this section we give a brief overview of the treatment of the initial-value problem and the form of the initial data. The essential feature of the data is that they consist of a time symmetric gravitational wave overlaid on an Einstein-Rosen bridge. In doing this we have superimposed two well-studied vacuum time symmetric spacetimes: the Schwarzschild solution, whose properties are completely known and for which several numerical studies in the 3+1 formalism have been done [23,14], and the Brill wave spacetime for time symmetric gravitational waves in which the initial-value problem has been extensively studied by Brill [11] and others [24,25], and its evolution studied by Eppley [26], Miyama [27], and Abrahams and Evans [28].

The initial-value problem consists of finding a three-metric and extrinsic curvature which satisfy the constraint equations (2) and (3). To date we have confined our research to the study of spacetimes which contain a surface of time symmetry. As is well known, the extrinsic curvature must vanish on a time symmetric surface and hence the momentum constraint will be satisfied identically on it.

This leaves us with only the Hamiltonian constraint $R = 0$, to be satisfied by γ_{ab} . Using a conformal decomposition technique for finding an appropriate three-metric and writing γ_{ab} in conformal form, $\gamma_{ab} = \Psi^4 \hat{\gamma}_{ab}$, gives

$$R = \Psi^{-4} \hat{R} - 8\Psi^{-5} \hat{\Delta} \Psi = 0, \quad (26)$$

where \hat{R} and $\hat{\Delta}$ are the scalar curvature and Laplacian associated with the conformal metric $\hat{\gamma}_{ab}$. The Hamiltonian constraint becomes the *linear* equation

$$\hat{\Delta} \Psi = \frac{1}{8} \Psi \hat{R}. \quad (27)$$

At this point one may choose the conformal metric and solve (27) for the conformal factor. We work in the (η, θ, ϕ) coordinates, in which the line element is chosen to take the ‘‘Brill wave’’ form

$$dl^2 = \Psi^4 [e^{2q}(d\eta^2 + d\theta^2) + \sin^2 \theta d\phi^2]. \quad (28)$$

As discussed in [3,4], the function $q(\eta, \theta)$ can be chosen freely, up to certain boundary and size conditions. The choice $q = 0$ produces the Schwarzschild solution, while a nonzero, nonspherical choice for q produces a distorted black hole. The Hamiltonian constraint (2) is transformed into

$$\frac{\partial^2 \Psi}{\partial \eta^2} + \frac{\partial^2 \Psi}{\partial \theta^2} + \frac{\partial \Psi}{\partial \theta} \cot \theta - \frac{1}{4} \Psi = -\frac{1}{4} \Psi \left(\frac{\partial^2 q}{\partial \eta^2} + \frac{\partial^2 q}{\partial \theta^2} \right). \quad (29)$$

This equation is written as a finite difference equation and solved using techniques described in Sec. III B.

In this work we have given q the form

$$q = f(\theta)g(\eta), \quad (30)$$

where g is an ‘‘inversion symmetric Gaussian’’

$$g = a \left(e^{-(g_+)^2} + e^{-(g_-)^2} \right), \quad (31)$$

with

$$g_+ = \frac{\eta + \eta_0}{w}, \quad g_- = \frac{\eta - \eta_0}{w}, \quad (32)$$

and

$$f = \sin^n \theta \quad (33)$$

with n an integer. The angular function f must vanish on, and be symmetrical through, $\theta = 0$, hence n must be even. The radial function g has three independent parameters a , η_0 , and w which specify its amplitude, range, and width.

As mentioned above we have chosen the conformal factor to be symmetric through the axis, equator, and throat. On the outer boundary we employ the Robin condition [29], which eliminates the monopole term in the asymptotic expansion of Ψ , so that the error on the outer boundary is only of order r^{-3} . The condition is

$$\frac{\partial \Psi}{\partial r} + \frac{\Psi - 1}{r} = 0 \quad (34)$$

or using the radial coordinate η

$$\frac{\partial \Psi}{\partial \eta} + \frac{1}{2} \Psi - \sqrt{\frac{m}{2}} e^\eta = 0. \quad (35)$$

Note that in spherical symmetry the Hamiltonian constraint has the exact solution

$$\Psi = \sqrt{2m} \cosh(\eta/2), \quad (36)$$

which is just the standard Schwarzschild solution written in these coordinates [14]. For numerical reasons we will usually factor Ψ into the form

$$\Psi = \sqrt{2m} \cosh(\eta/2) \Psi', \quad (37)$$

and solve the Hamiltonian constraint for Ψ' .

E. Kinematics

In numerical relativity there are two rather distinct aspects to the construction of spacetime coordinate systems. The first is the problem of how to lay down spatial coordinates on the initial slice, and the second is

the construction of subsequent slices and the mapping of these spatial coordinates onto them. The two problems are somewhat intertwined in the sense that both involve physical as well as numerical and computational considerations.

1. Spatial coordinates

Despite the freedom inherent in the shift vector, the choice of spatial coordinates on the initial slice is important because often one does not employ a shift or because the shift is used for other reasons, not directly related to the kinematics (as is, in fact, the case in this work). Hence these coordinates must be chosen with some care.

As an example we look at two possible choices for the spatial coordinates in the black hole plus Brill wave spacetime. The first are the usual spherical polarlike coordinates in which the spatial line element appears as

$$dl^2 = \Psi'^4 (A' dr^2 + B' r^2 d\theta^2 + 2C' r dr d\theta + D' r^2 \sin^2 \theta d\phi^2), \quad (38)$$

and the second are the coordinates (η, θ, ϕ)

$$dl^2 = \Psi^4 (A d\eta^2 + B d\theta^2 + 2C d\eta d\theta + D \sin^2 \theta d\phi^2). \quad (39)$$

These systems both have the numerically desirable property that the isometry surface is a constant coordinate surface, $r = m/2$ and $\eta = 0$, respectively. Reflection through the isometry surface is assumed to be of the form $r \rightarrow m^2/4r$ and $\eta \rightarrow -\eta$. The isometry operator determines the inner boundary condition for the three-metric components (as discussed in Sec. II C) and for a *conformally flat* three-metric in the (r, θ, ϕ) coordinates the boundary condition on Ψ [determined in the same way as Eq. (12)] turns out to be

$$\left(\frac{\partial \Psi}{\partial r} + \frac{\Psi}{m} \right) \Big|_{r=m/2} = 0. \quad (40)$$

This “anti-Robin” condition causes problems in solving the Hamiltonian constraint [29]. It is “anti-Robin” because the “outward” pointing unit normal is pointing into the computational domain (unlike the situation on the outer boundary).

Another issue is associated with the finite difference solution of hyperbolic equations. It is a general rule of thumb that in order to propagate the solutions most accurately the computational grid zones should be of uniform size. That is, the zones should be as near to square as possible and all of the same area in the computational domain. In abiding by this rule we should choose Δr or $\Delta \eta$ to be as close to $\Delta \theta$ as possible. Now, on an asymptotically flat slice both Ψ' and A' will tend toward unity at the outer edge of the grid and so points evenly spaced in r will also be evenly spaced in proper distance. This means that a relatively large number of zones will be used to cover the region near the grid edge and if the grid points are evenly spaced in r this coverage comes at the expense of coverage in the interior where we expect most of the interesting dynamics to occur. This is

overcome by the use of the logarithmic coordinate η in which the proper distance between points evenly spaced in η increases exponentially as η increases. Hence a grid covered with such evenly spaced points will have a larger proportion of the total number of points in the dynamically interesting region than a grid evenly covered with points in the r coordinate.

This in turn suggests a drawback to the η coordinates. Evans [30] has cited a figure of 50 zones per wavelength needed to accurately propagate a wave. Since the grid zones are being stretched in proper length as η increases, there will be a critical value of η at which the number of grid zones spanning a wavelength will drop below 50. The specific three-metric of a particular slice will determine exactly where this happens, but for an asymptotically flat three-metric we may make an approximation as follows. In the wave zone the number of zones per wavelength, $n = \lambda/\Delta r$, in the r coordinates will be constant no matter where the wave is and on a grid evenly spaced in $\Delta \eta$ we have $n = \lambda/r\Delta \eta$. Therefore the r value where the wave spans exactly n zones over a grid evenly spaced in η is $\lambda/n\Delta \eta$. Currently our “high resolution” runs are done with 200 radial zones with an outer boundary at $\eta = 6$ hence $\Delta \eta = 0.03$. If we desire 50 zones per wavelength the outer limit for very accurate propagation of a $\lambda = 17M$ wave (roughly what we expect from a black hole of mass M) is about $15M$. By $r = 50M$, we are down to 15 zones per wavelength. This loss of resolution at large radii can lead to poor propagation and reflection of the waves, as noted in Ref. [4] and shown here in Fig. 1. In practice, at this resolution, good propagation is seen out to about $50M$, where degradation of the waveform begins to occur. See [4] for more details.

Another disadvantage of the concentration of zones near the isometry surface in the η coordinates is connected with the phenomena of “grid sucking” associated with most singularity avoiding lapse function choices.

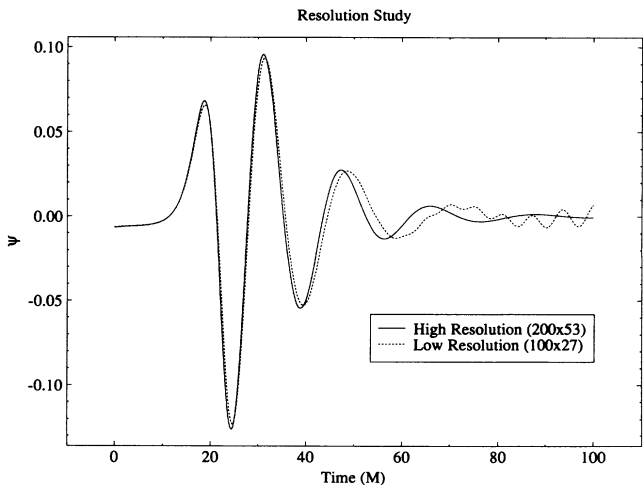


FIG. 1. This figure shows the same waveform as the previous figure but at 100 and 200 radial zone resolution. The lower resolution calculation suffers from oscillations at late times, as discussed in the text.

This is the problem whereby zones are pulled through the event horizon due to the gravitational focusing of timelike geodesics. The problem is that in the η coordinates more zones as a percentage of the whole will be sucked through the event horizon than if the hypersurfaces were evenly covered in the r coordinates. These zones are effectively gone from the calculation as far as the exterior of the horizon is concerned. For the maximally sliced Schwarzschild solution with $\beta^a = 0$ about 40% of the zones fall through the horizon in an evolution to $t = 80M$ if the outer boundary is at $\eta = 6$. If the initial slice is covered in the r coordinates with the same number of zones this figure is reduced to 2%. This problem may be circumvented by using an apparent horizon boundary condition, where a shift is used to maintain a fixed coordinate position for the horizon [31]. This approach has worked well in spherical symmetry, and work is underway to extend this technique to more general spacetimes.

2. Slicing conditions

Given the absence of rotation and electric charge, we expect that the black hole plus Brill wave spacetimes each have the same singularity structure as the Schwarzschild spacetime. That is, they contain a spacelike singularity in the future of the initial slice. The initial slice always contains a trapped surface [3] and so it will also contain an event horizon assuming cosmic censorship holds [32]. A singularity avoiding slicing condition is essential if we allow the slicing to intersect an event horizon and we insist on computing the region of spacetime inside the horizon.

We have used maximal slicing almost exclusively to foliate the spacetimes. Maximal slicing has been used extensively in numerical relativity for several reasons: considerable analytic work has been done delineating its singularity avoiding properties [23,10,33–36]; it was used in early numerical work which centered on computing black hole spacetimes with Einstein-Rosen bridges, and it is conveniently computed from the three-metric and extrinsic curvature. Finally it can be encoded into a stable numerical algorithm. Here we give only a brief sketch of its use.

Maximal slices (i.e., hypersurfaces with maximal volume) are characterized by the vanishing of their mean curvature

$$\text{tr}K \equiv \gamma^{ab}K_{ab} = 0. \quad (41)$$

The evolution equation for $\text{tr}K$ may be computed from Eqs. (4) and (5) and the maximal slicing condition is obtained by setting $\text{tr}K = \partial_t \text{tr}K = 0$:

$$\partial_t \text{tr}K = -D^a D_a \alpha + \alpha R = 0, \quad (42)$$

or, using the Hamiltonian constraint,

$$D^a D_a \alpha = \alpha K^{ab} K_{ab}. \quad (43)$$

This latter form tends to be better behaved numerically, and is the form used in the code.

The properties of equations of this type have been explored at length elsewhere [37] and for our purposes it is sufficient to point out a few elementary things. $K^{ab}K_{ab}$ is a positive indefinite quantity in the spacetimes considered in this work. When this is the case it is known that solutions to (43) exist, are unique, and are in a sense well behaved [37]. Also the equation is linear in α and the numerical solution of such equations has been studied extensively [38].

Given an initial $\text{tr}K = 0$ slice, a subsequent one may be constructed by specifying appropriate boundary conditions on the lapse and solving (43). In this work we use the mixed von Neumann/Dirichlet conditions:

$$\left. \frac{\partial \alpha}{\partial \eta} \right|_{\eta=0} = 0, \quad \alpha(\text{outer boundary}) = \tanh(\eta/2), \quad (44)$$

which determine the isometry sign across the throat (see Sec. II C) and the Schwarzschild-like behavior at the grid edge.

3. Shift vector conditions

Ever since the work of Smarr [39] and Smarr and Eppley [18] on the axisymmetric two black hole collision it has been known that general three-metrics are prone to developing instabilities on or near the axis of symmetry. These instabilities have severely hampered progress on the two black hole collision; in fact the two black hole spacetimes of Smarr and Eppley were usually stopped after about 40–60M off the initial slice because of numerical problems caused by the uncontrolled growth of certain metric and extrinsic curvature components near the axis [18]. (Recent progress on this subject has been reported in Ref. [2].) Our initial attempts to evolve the distorted black hole spacetimes described above with a general three-metric of the form (9) also suffered from a similar instability along the symmetry axis (see Sec. IV B).

As we detail in Sec. IV B this instability can be controlled somewhat by forcing the coordinates to remain spatially orthogonal at all times. This is accomplished by the introduction of a shift which makes γ_{12} vanish. Since our initial data is already of this form we need only introduce a shift such that

$$\partial_t \gamma_{12} = -2\alpha K_{12} + D_\eta \beta_\theta + D_\theta \beta_\eta = 0. \quad (45)$$

Expanding the covariant derivatives and writing the equation for the contravariant components we have

$$2\alpha H_c = B \frac{\partial \beta^\theta}{\partial \eta} + A \frac{\partial \beta^\eta}{\partial \theta} \quad (46)$$

(here we have already used $C = 0$). This gives us one equation to determine both components of β^a . A further restriction is made by requiring the shift to be the “gradient” of a “potential” Ω ,

$$\beta^\eta = \frac{\partial \Omega}{\partial \theta}, \quad \beta^\theta = \frac{\partial \Omega}{\partial \eta}, \quad (47)$$

which yields an elliptic equation for Ω :

$$2\alpha H_c = B \frac{\partial^2 \Omega}{\partial \eta^2} + A \frac{\partial^2 \Omega}{\partial \theta^2}. \quad (48)$$

This equation is then solved in the usual way: by substituting finite difference approximations for the derivatives of Ω and using a linear system solver on the result. Given the boundary conditions (23) and (24) it can easily be seen that Ω must be antisymmetric across the axis, equator, and throat. The condition $\Omega = 0$ is used at the outer boundary where we have found that it makes both the shift and its gradients smoothly go to zero. The effects of this gauge on the instability are discussed in Sec. IV B.

This method has proved to be convenient and successful in evolving the black hole plus gravitational wave spacetime. However, an additional degree of freedom in the shift could be used for other purposes. For example, one could use the shift to keep the three-metric diagonal, as we have, and also enforce another condition. One choice would be to require the metric to have the “quasi-isotropic” form [30], which in our system would require $A = B$. However when this condition is used in the Schwarzschild spacetime it produces an inward pointing shift which forces a large portion of the grid inside the event horizon [5].

III. THE NUMERICAL ALGORITHMS

In this section we will discuss the different algorithms we have used for the evolution of the Einstein equations, and for the solution of the elliptic equations arising from our gauge choices. Following on the work reported in Ref. [14] we have implemented three different time explicit evolution schemes in the code: leapfrog with half-time-step extrapolation, MacCormack, and Brailovskaya. We will summarize the three methods below in Sec. III A, and compare results of the methods in Sec. IV. In Sec. III B we discuss the solution of the elliptic equations.

A. Hyperbolic equation (evolution) algorithms

The evolution equations in 3+1 form are discussed in detail in Sec. II A above. For brevity we will write them here in schematic form:

$$\partial_t \gamma = -2\alpha K \quad (49)$$

and

$$\partial_t K = \alpha(K^2 + R) + \nabla \nabla \alpha. \quad (50)$$

The symbols γ , K , and R are symbolic of the metric quantities γ_{ab} , K_{ab} , and the Ricci tensor, while $\nabla \nabla \alpha$ represents the covariant Hessian of the lapse. The numerical grid upon which the finite differencing is accomplished has fixed step sizes in both temporal and spatial zoning. In the finite differenced form of the evolution equations to follow, the spatial steps will be labeled by the letter i , while the time steps will be labeled by n .

We start with the leapfrog method. This is perhaps the most commonly used method for evolving hyperbolic systems. The usual leapfrog method has the “momen-

tumlike” quantities (in this case K_{ab}) offset from the “fieldlike” quantities (γ_{ab}) by 1/2 of a time step so that the time derivatives are properly centered. Thus, one can write the evolution system (49) and (50) as

$$\gamma_i^{n+1/2} = \gamma_i^{n-1/2} - 2\alpha_i^n K_i^n \Delta t \quad (51)$$

and

$$K_i^{n+1} = K_i^n + \{\alpha_i^n [(K_i^n)^2 + R_i^{n+1/2}] - (\nabla \nabla \alpha)_i^n\} \Delta t. \quad (52)$$

However, this introduces first-order errors due to the nonlinear term $(K_i^n)^2$. This problem can be cured by extrapolating the quantity K_i to the time slice labeled by $n+1/2$ using the second-order accurate formula

$$K_i^{n+1/2} = \frac{3}{2} K_i^n - \frac{1}{2} K_i^{n-1}. \quad (53)$$

Then the second-order accurate, extrapolated leapfrog method can be written as

$$\gamma_i^{n+1/2} = \gamma_i^{n-1/2} - 2\alpha_i^n K_i^n \Delta t \quad (54)$$

and

$$K_i^{n+1} = K_i^n + \{\hat{\alpha}_i^{n+1/2} [(K_i^{n+1/2})^2 + R_i^{n+1/2}] - (\nabla \hat{\nabla} \alpha)_i^{n+1/2}\} \Delta t. \quad (55)$$

This method works very well, as we discuss in Sec. IV.

Now we turn to two predictor-corrector methods, the MacCormack and Brailovskaya schemes. These schemes are discussed in Ref. [40] where they are applied to Burger’s equation written in flux conservative form. Because the Einstein equations are not in this form, the standard analysis for the stability, dissipation, and dispersion properties of these methods does not apply directly. The treatment of the time derivatives in the Einstein equations can be carried over directly, but the structure of spatial derivatives is much more complex than found in Burger’s equation. These methods worked very well in spherical symmetry, as reported in Ref. [14]. In fact, they were found to be superior to the extrapolated leapfrog method described above. However, in spherical symmetry there is only a longitudinal part of the field; the transverse, or wave part, is absent. This extra degree of freedom in the equations will pose some difficulty for the predictor-corrector methods as we will discuss in Sec. IV.

Both of these schemes have two steps in the evolution to the next time slice. The MacCormack predictor-corrector scheme is written as

$$\tilde{\gamma}_i^{n+1} = \gamma_i^n - 2\alpha_i^n K_i^n \Delta t \quad (56)$$

and

$$\tilde{K}_i^{n+1} = K_i^n + \{\alpha_i^n [(K_i^n)^2 + R_i^n] - (\nabla \nabla \alpha)_i^n\} \Delta t \quad (57)$$

constitute the first, or predictor step, while

$$\gamma_i^{n+1} = \frac{1}{2} [\tilde{\gamma}_i^n + \gamma_i^n - 2\alpha_i^n \tilde{K}_i^n \Delta t] \quad (58)$$

and

$$K_i^{n+1} = \frac{1}{2}[\tilde{K}_i^n + K_i^n + \{\alpha_i^n[(\tilde{K}_i^{n+1})^2 + \tilde{R}_i^{n+1}] - (\nabla\tilde{\nabla}\alpha)_i^{n+1}\}]\Delta t \quad (59)$$

constitute the second, or corrector step. This method is somewhat different from other methods in that for the predictor step the first spatial derivatives of the metric appearing in the Ricci tensor and Hessian of the lapse can be determined by forward differencing: $\partial_\eta \gamma_i^n = (\gamma_{i+1}^n - \gamma_i^n)/\Delta\eta$. In the corrector equations these derivatives are calculated using backward differencing: $\partial_\eta \gamma_i^n = (\gamma_i^n - \gamma_{i-1}^n)/\Delta\eta$. An alternative method is to backward difference at the predictor level and forward difference the corrector equation. However, in this code we have used centered derivatives in both predictor and corrector. Second derivatives are always centered. We also note that in other applications [41] centered spatial derivatives have been used in both the predictor and corrector steps with satisfactory results, as long as time steps were kept sufficiently small. Results from the MacCormack method will be discussed further in Sec. IV E.

Finally we turn to the Brailovskaya predictor-corrector method which we have also used to evolve the Einstein equations. This method uses a centered differencing scheme for spatial derivatives in both the predictor and corrector equations:

$$\tilde{\gamma}_i^{n+1} = \gamma_i^n - 2\alpha_i^n K_i^n \Delta t \quad (60)$$

and

$$\tilde{K}_i^{n+1} = K_i^n + \{\alpha_i^n[(K_i^n)^2 + R_i^n] - (\nabla\tilde{\nabla}\alpha)_i^n\}\Delta t \quad (61)$$

are the predictor steps, while

$$\gamma_i^{n+1} = \gamma_i^n - 2\alpha_i^n \tilde{K}_i^n \Delta t \quad (62)$$

and

$$K_i^n = K_i^n + \{\alpha_i^n[(\tilde{K}_i^{n+1})^2 + \tilde{R}_i^{n+1}] - (\nabla\tilde{\nabla}\alpha)_i^{n+1}\}\Delta t \quad (63)$$

are the corrector steps. This method is formally first order in time and we shall see in Sec. IV E that it performs slightly less well than the leapfrog and MacCormack methods. A full comparison of these methods will be presented in Sec. IV E.

These explicit finite difference methods for evolving hyperbolic systems require certain restrictions on the size of the time step for stability. In analogy to the second-order wave equation in flat space, the Courant stability condition for a wave traveling in the radial direction would be

$$\Delta t < \sqrt{\left| \frac{g_{\eta\eta}}{g_{tt}} \right|} \Delta\eta. \quad (64)$$

This condition generally applies to the leapfrog scheme described above when considering a linear wave equation, but more restrictive time step requirements are found for

the MacCormack and Brailovskaya methods [41]. The Courant condition becomes more complicated when a shift vector is used. Furthermore, the strict stability analysis for complex nonlinear equations such as the Einstein equations would be very complicated, and has not been performed.

In spite of these deficiencies in the analysis, the standard formula (64) can provide useful guidance in choosing a time step, as long as the shift vector remains small [31]. In practice, we have generally chosen $\Delta t = \Delta\eta$, which is usually far below the Courant limit. Significantly larger time steps can be used in some cases, although with reduced accuracy. An adaptive time step routine using both the Courant limit and restriction on time derivatives of the metric functions as a guide could be used to make our code more efficient, but this approach has not yet been explored. The results quoted in this paper and in [4] were obtained with $\Delta t = \Delta\eta$.

B. Elliptic equation algorithms

The solution of the elliptic equations arising in this calculation is the most CPU intensive part of the numerical integration of the Einstein equations. Our system requires that we solve the Hamiltonian constraint as described in Sec. II D for the initial data, and then during the evolution elliptic equations are used to provide both the lapse and shift functions, as described in Secs. II E 2 and II E 3. Here we discuss a variety of techniques that we have explored for solving these equations accurately and efficiently.

The equations for the lapse, α (43), and shift vector potential, Ω (48), and the conformal factor, Ψ (29), are all second-order-linear elliptic partial differential equations that can be written in the general form

$$a_{11} \frac{\partial^2 x}{\partial \eta^2} + a_{12} \frac{\partial^2 x}{\partial \eta \partial \theta} + a_{22} \frac{\partial^2 x}{\partial \theta^2} + a_{01} \frac{\partial x}{\partial \eta} + a_{02} \frac{\partial x}{\partial \theta} + a_{00} x = b(\eta, \theta), \quad (65)$$

where $x(\eta, \theta)$ is a scalar function of the independent coordinate variables. The coefficients a_{11} , a_{12} , etc., are functions of both η and θ and are determined by the three-metric and various partial derivatives of the three-metric with respect to the spatial coordinates.

In order to solve elliptic equations numerically, the usual approach is to approximate the derivatives with finite difference operators and solve the resulting system of simultaneous equations. Fortunately, our elliptic equations are linear, so the resulting algebraic system is also linear. (Nonlinearities are typically handled by linearizing and iterating, so the technique is essentially the same.) There are many ways of writing finite difference operators, so the resulting system is not a unique representation of the elliptic equations. However using central differences to represent first and second partial derivatives,

$$\left. \frac{\partial x}{\partial \eta} \right|_{i,j} = \frac{x_{i+1,j} - x_{i-1,j}}{2\Delta\eta}, \quad (66)$$

$$\left. \frac{\partial^2 x}{\partial \eta^2} \right|_{i,j} = \frac{x_{i+1,j} - 2x_{i,j} + x_{i-1,j}}{(\Delta \eta)^2}, \quad (67)$$

$$\left. \frac{\partial x}{\partial \theta} \right|_{i,j} = \frac{x_{i,j+1} - x_{i,j-1}}{2\Delta \theta}, \quad (68)$$

$$\left. \frac{\partial^2 x}{\partial \theta^2} \right|_{i,j} = \frac{x_{i,j+1} - 2x_{i,j} + x_{i,j-1}}{(\Delta \theta)^2}, \quad (69)$$

the elliptic partial differential equation (PDE) leads to an algebraic equation at each of the N grid points (i, j) (where i labels η nodes and j labels θ nodes) that couple values of the function x at that grid point with the values of the function at the nearest neighbor grid points,

$$an x_{i+1,j} + ae x_{i,j+1} + ac x_{i,j} + aw x_{i,j-1} + as x_{i-1,j} = b_{i,j}, \quad (70)$$

where an , as , ae , and aw correspond to the north, south, east, and west directions from the central point, ac , of the stencil on the grid:

$$\begin{aligned} an &= \frac{a_{22}}{(\Delta \theta)^2} + \frac{a_{02}}{2\Delta \theta}, \\ ae &= \frac{a_{11}}{(\Delta \eta)^2} + \frac{a_{01}}{2\Delta \eta}, \\ ac &= a_{00} - 2\frac{a_{11}}{(\Delta \eta)^2} - 2\frac{a_{22}}{(\Delta \theta)^2}, \\ aw &= \frac{a_{11}}{(\Delta \eta)^2} - \frac{a_{01}}{2\Delta \eta}, \\ as &= \frac{a_{22}}{(\Delta \theta)^2} + \frac{a_{02}}{2\Delta \theta}, \end{aligned}$$

where all of the A 's are evaluated at the central (i, j) grid point. All of the elliptic equations appearing in the code have $a_{12} = 0$.

The standard form for a set of linear equations is that of a matrix equation $\mathbf{Ax}=\mathbf{b}$, where \mathbf{A} is an $N \times N$ square matrix containing all the finite difference coefficients, \mathbf{x} is a vector of N elements consisting of all the unknowns, and \mathbf{b} (the right-hand side) is a vector containing all the source terms and the given boundary values. By using a new index $k = (i - 1) \times (j_{\max}) + j$ that counts grid points along successive constant grid lines we can order the equations such that they have this form. In this way we generate a standard matrix form of the problem where \mathbf{A} is now a very sparse matrix with diagonal structure as shown in Fig. 2. For details on this procedure see Press *et al.* [38].

Once the linear system of equations has been written in the sparse matrix form we must solve the matrix equation for the unknown values of the scalar function. We have explored a number of different methods, including direct, iterative, and multigrid methods.

C. Numerical methods

In this section we review the different methods used to solve the linear elliptic equations for the scalar functions

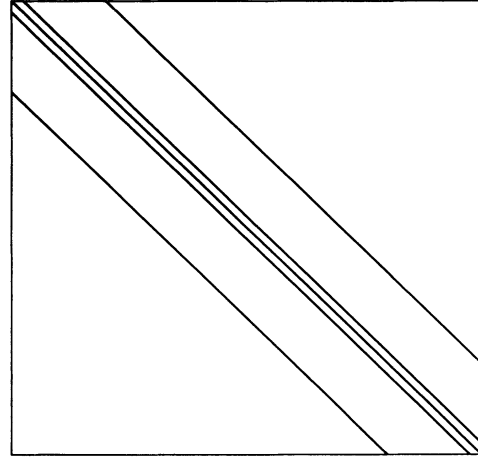


FIG. 2. The sparsity structure of the coefficient matrix for the ordered set of equations arising from the elliptic systems is shown.

$\alpha(\eta, \theta)$, $\Omega(\eta, \theta)$, and $\Psi(\eta, \theta)$ and make comments about particular implementations of those methods and how they affect the overall performance of the code.

1. Direct methods

The great advantage of the direct solvers is that they obtain the solution in a fixed number of operations. These methods are well described by Press *et al.* [38]. However, since we are considering large systems, these methods are subject to the accumulation of round-off errors. Also, since we are considering massively parallel and/or vector supercomputer architectures, they suffer because the backward and forward substitutions implicit to these methods are nonparallelizable, nonvectorizable operations and will execute at scalar speeds. For these reasons iterative solvers are more efficient in our case.

A multifrontal method combined with incomplete factorization of the coefficient matrix for solving large linear systems was used and its implementation was written by Boeing Computer Services, Inc. (BCSLIB-EXT).

2. Iterative methods

Since the advent of computers with sufficient memory to compute large problems, iterative solvers have undergone significant development and many mature iterative methods are now available. Most of these techniques fall under the headings of relaxation methods or gradient (Krylov subspace [42]) methods.

Relaxation methods can involve the simplest Jacobi or Gauss-Seidel techniques to more sophisticated simultaneous overrelaxation (SOR) algorithms [38]. These techniques successively solve the system of equations for the unknowns using each solution as an approximation for the next iteration. While the relaxation methods can perform quite well, they do not have a finite termination criterion; they are only guaranteed to converge as the it-

eration number approaches infinity. These methods are useful when combined with multigrid methods (see below).

Many of the *gradient methods* in use today are based on the conjugate gradient (CG) method of Hestenes and Steifel [43] for symmetric positive-definite systems (i.e., \mathbf{A} is a symmetric matrix), or extensions of the CG method to apply to nonsymmetric systems. Essentially the conjugate gradient method minimizes a quadratic function of the form

$$f(\mathbf{u}) = \frac{1}{2} \mathbf{x}^T \cdot \mathbf{A} \cdot \mathbf{x} - \mathbf{x}^T \cdot \mathbf{b}$$

by calculating the gradient along a certain direction and then minimizing this quantity. This is equivalent to solving the original matrix equation.

Some specialized conjugate gradient methods applicable to nonsymmetric matrices are (i) conjugate gradients applied to the normal equations (CGNR), (ii) biconjugate gradients (BiGC) [44], (iii) (bi)conjugate gradients squared [(Bi)CGS] [45], and (iv) BiCGStab [46]. Other Krylov subspace methods include the generalized minimal residual (GMRES) method [47] and the generalized conjugate gradient (GCG) method [48], but we have not applied these methods to our problem.

A great advantage of the Krylov subspace methods is that they are guaranteed to converge in a finite number of iterations. Generally the maximum number of iterations will be the number of unique eigenvalues of the coefficient matrix \mathbf{A} . However, the convergence rates of the various Krylov subspace methods can vary greatly, as can the memory requirements. The second advantage to these methods is that they can generally be implemented in a parallelizable and vectorizable fashion which makes them particularly appealing for use on parallel and/or vector supercomputers.

Finally, all iterative techniques can benefit greatly from effective preconditioning. Here, the matrix equation $\mathbf{A}\mathbf{x}=\mathbf{b}$ is modified to produce an equivalent system of equations of the general form

$$\mathbf{QAP}^{-1}\mathbf{x} = \mathbf{Qb} \quad (71)$$

and then perform the iterative algorithm on the system

$$\mathbf{M}\mathbf{y} = \mathbf{d}, \quad (72)$$

where

$$\mathbf{M} = \mathbf{QAP}, \quad (73)$$

$$\mathbf{y} = \mathbf{P}^{-1}\mathbf{x}, \quad (74)$$

$$\mathbf{d} = \mathbf{Qb}. \quad (75)$$

The preconditioning is most effective when the matrix \mathbf{M} is nearly the identity matrix, and when the procedure for implementing the preconditioning is not computationally expensive for the machine architecture being used.

One of the Krylov space methods used was a generalized conjugate residual (GCR) method using modified incomplete LU (MILU) decomposition as a preconditioner. This method is implemented by Scientific Computing Associates, Inc., in its PCGPAK package and was the first of

the conjugate gradient methods employed in the code. However, being a general method, there was a great deal of overhead associated with this particular implementation. It was not highly vectorized and ran at nearly scalar speeds on a vector processor.

A BiCGS algorithm with a least squares polynomial (LSP) preconditioner was also used. This solver was written as part of the ITPACK project of the Center for Numerical Analysis at The University of Texas at Austin. The method was one of many included in the NSPCG package.

The final conjugate gradient method to be used was a BiCGStab algorithm written by one of us (J.T.) at the National Center for Supercomputing Applications; the CG-based algorithm was developed by Henk Van der Vorst [46]. This is an advancement over the BiCGS algorithm. However, no effective preconditioning has yet been used, although code development is currently under way in this area.

3. Multigrid

It is well known that iterative solutions to large matrix equations obtained by the use of relaxation methods have the advantage that they reduce the high frequency components in the error but at the same time converge very slowly to a solution in the low frequency components. Multigrid methods provide a means for overcoming the slow convergence while taking advantage of the smoothing that results from the relaxation. Since the convergence of a relaxation method improves if the initial estimate of the solution is close to the solution itself, multigrid solves the problem on a less computationally intensive course grid and interpolates that solution onto the fine grid to provide a better initial guess.

One begins with the matrix equation $\mathbf{A}^h \mathbf{x}^h = \mathbf{b}^h$, obtained from the finite differencing of an elliptic PDE $\mathcal{A}x = b$ having a coarseness h . (Here \mathcal{A} represents the differential operator acting on the continuous function x .) This grid is generally of the same coarseness on which the evolution equations are solved. Using a simple relaxation technique one can obtain a relatively smooth solution $\bar{\mathbf{x}}^h$ after a few iterations. A residual $\mathbf{r}^h = \mathbf{b} - \mathbf{A}^h \bar{\mathbf{x}}^h$ is calculated and this is *restricted* to a grid of greater coarseness h' (generally $h' = 2h$) by the restriction operator $\mathbf{R}_h^{h'}$ ($\mathbf{r}^{h'} = \mathbf{R}_h^{h'} \mathbf{r}^h$). The low frequency components in the error on the fine grid now become high frequency components on the course grid and further smoothing using a relaxation method can be employed on the course grid to further eliminate the new high frequency components.

A correction $\mathbf{c}^{h'}$ is then obtained to the solution on the course grid and that can be *interpolated* onto the fine grid by the interpolation operator $\mathbf{I}_h^{h'}$ to obtain a correction on the fine grid, $\mathbf{c}^h = \mathbf{I}_h^{h'} \mathbf{c}^{h'}$. The interpolated correction when added to $\bar{\mathbf{x}}^h$ can be smoothed by relaxation to obtain an improved fine grid solution \mathbf{x}^h .

Multigrid therefore solves the problem on multiple scales and consists of three operations (i) smoothing, (ii) restriction (moving from fine to course grids), and (iii) interpolation or prolongation (moving from course

TABLE I. Timing results for black hole spacetime evolution. Data is for a 200×55 grid run to $t = 100M$ on a single Cray Y-MP processor.

	Time (min)	Speedup	MFLOPS	Zone (cycles/sec)	Memory size (MW)
GCR (PCGPAK)	280.5	1.0	21	4503	3.2
Direct (BCSLIB)	174.2	1.6	36	7251	2.6
NSPCG	120.5	2.3	176	10 483	1.0
UMGS2	23.2	12.1	73	54 447	1.4
BiCGStab	18.3	15.3	213	69 025	1.0

to fine grids). Different methods for smoothing (Jacobi, Gauss-Seidel, SOR) can be used as can different restriction (full-weighting, half-weighting with injection) and interpolation (bilinear, cubic spline) methods.

The multigrid method used with our code was provided by Steven Schaffer of New Mexico Technical Institute [49] (UMGS2). UMGS2 is a semicoarsening multigrid code. This differs from full multigrid as described by only performing the coarsening along only one of the dimensions of the grid. This provides an algorithm that is much easier to implement, yet retains the efficiency of using multigrid. We perform the coarsening only along the θ direction which since the solution is more smooth in that direction.

D. Performance results

Each method was used to solve the same problem, the numerical evolution of a black hole plus gravitational wave spacetime. The equations for the lapse α (43) and shift potential Ω (48) are solved on each time slice in the evolution. Since the coefficients in these equations are time dependent, a different pair of elliptic equations is solved on each time step (i.e., the spatial dependence of each coefficient is different on each time step).

1. Performance statistics

For the iterative solvers, iteration ceased when the Euclidean norm of the residuals reached a certain tolerance. The Euclidean norm, or 2-norm, of the residuals is given by

$$\| \mathbf{r} \|_2 = \langle \mathbf{r}, \mathbf{r} \rangle^{\frac{1}{2}} = \sqrt{\mathbf{r}^T \mathbf{r}}. \quad (76)$$

The residual at the m th iteration is given by

$$\mathbf{r}_m = \mathbf{b} - \mathbf{A} \mathbf{x}_m, \quad (77)$$

where \mathbf{x}_m is the approximation to \mathbf{x} at the m th iteration. Iteration stopped for the solution of each equation when

$$\| \mathbf{r}_m \|_2 < 1.0 \times 10^{-8}$$

TABLE II. Timing results for black hole spacetime evolution. Data is for a 400×106 grid run to $t = 25M$ on four Cray Y-MP processors.

	CPU time (min)	Elapsed time (min)	Concurrency	MFLOPS	Zone (cycles/sec)	Memory size (MW)
BiCGStab	95.0	24.2	3.92	773	99 011	3.1

was satisfied.

Table I summarizes the performance statistics of the code for each solver, showing the UMGS2 and BiCGStab algorithms to be the best for these particular equations. The numbers given are for a complete run of the entire code (which includes the solution of the hyperbolic equations as well) for identical problems to $t = 100M$ (6667 time steps, i.e., 13 335 elliptic equations are solved) with 200 radial zones and 55 angular zones. The codes were run on a single processor of NCSA's Cray Y-MP4/464. While the MFLOPS (million floating point operations per second) rates for the different solvers vary greatly, the more important results are *total run time of the code* and *zone cycles/second* (a measure of how many grid points per second can be evolved).

We have also begun to experiment with parallelization of our code on the Cray architecture. As an initial test the BiCGStab version of the iterative solver was rewritten to distribute the computationally intensive tasks across multiple processors and our initial numbers are very encouraging. Table II shows the results for evolving the same spacetime as above, but with twice the resolution (i.e., 400 radial zones and 106 angular zones). The concurrency is 3.92 (with a maximum of 4.00). Parallelization of the code will allow us to run the code in approximately one quarter the amount of time previously and means we have obtained a final speedup of approximately 60 times compared to using GCR solver on a single processor.

IV. CODE TESTS

Any numerical code must undergo thorough testing in various regimes where results are known, before it can be trusted to explore unknown territory. In this section we present a number of numerical results which provide tests of various aspects of the code. The 3+1 formalism of the Einstein equations naturally divides the problem into two parts: finding an initial data set consistent with the constraint equations, and then evolving that data set forward in time. We discuss both aspects of our code here.

A. Initial data

The initial data set is computed by solving the Hamiltonian constraint, as described in Sec. IID and in much more detail in Refs. [3,5]. In Ref. [3] the convergence of the solution as a function of grid resolution is discussed. The system is approximated by using second-order accurate finite difference approximations to the resulting elliptic equation, and solved using the techniques discussed in Sec. IIIB. As discussed in Ref. [3], the convergence was of second order in the grid spacing (coordinate intervals), and errors were not very sensitive to the particular solver used since the tolerances were set very low. For more details on convergence rates and error measurements and for an analysis of the physical content of the initial data please refer to Refs. [3,5].

B. Code stability: Diagonal vs general three-metric

Once initial data have been obtained, one can use the evolution equations along with the gauge conditions to solve the full Einstein equations. As is typical with hyperbolic systems, however, the numerical solution is prone to developing instabilities. As discussed in Sec. IIE3, an instability associated with the axis of symmetry has hampered many efforts to compute axisymmetric black hole spacetimes. Not surprisingly, the same type of instability is present in our code.

In spherical polar coordinates, the axis of symmetry ($\theta = 0$) is the location of a coordinate singularity. Since any small errors away from the regularity of the metric coefficients are multiplied by powers of $(\sin \theta)^{-1}$, near the symmetry axis care must be taken to obtain very accurate solutions in the vicinity of $\theta = 0$. The first issue to resolve is where to place grid zones relative to this axis. We have tried two approaches. One is to place grid zones so that they straddle the axis, to avoid directly calculating sensitive quantities where coordinate singularities exist. The other is to place a zone directly on the axis and treat it in a special way, by using l'Hopital's rule to derive a regularized set of evolution equations just for the axis itself. Separate codes have been developed for each of these approaches. In both cases, with a general axisymmetric metric, the instability is present. For a detailed discussion of the nature of the instability, its rate of growth, propagation across the grid, etc., see [5].

The instability is rooted in certain delicate terms in the evolution equations that on casual inspection would appear to blow up on the symmetry axis. The most egregious of these terms appear in the expressions for the Ricci tensor (see Appendix A). Although some of these terms may blow up individually near the axis, suitable combinations will cancel analytically in the limit as one approaches the axis so that the evolution equations do not actually contain singularities. The difficulty is that slight numerical errors will ruin the delicate cancellations. Small errors are divided by terms that vanish on the axis, leading to numerical instabilities. The off diagonal expressions contain the most damaging of such terms in the evolution equations. If we eliminate the off diagonal metric function C from the evolution equations,

many of these terms will disappear.

In our code we have eliminated the off diagonal three-metric component C by implementing the shift vector discussed in Sec. IIE3. In the code this condition is implemented by assuming $C = 0$ exactly in the evolution equations. If one allows C to evolve, the shift does not exactly cancel its evolution. The code is still unstable but the time scale for the instability to seriously degrade an evolution is shorter. With $C = 0$ enforced throughout the evolution the code is stable. If one repeats the spherically symmetric runs described above then what one finds is a very small, smooth, shift potential which has a maximum of order $10^{-11}M^{-1}$ near $\eta = 1.5$ and $\theta = \pi/4$. The extrinsic curvature component H_C is *not* smooth; it shows some erratic behavior near the axis. However, this behavior does not grow or propagate, remaining at very low levels ($10^{-9}M^{-1}$) even to the end of a long ($t = 100M$) run. Note that with a shift vector the code is using spatial derivatives of H_C in the evolution equations. If one adds only a very small amount of angular dependence to the initial data (say $a = 0.001$) then H_C evolves normally and the erratic behavior is not visible in the solution.

There are other approaches to solving problems created by coordinate singularities. Evans has developed a method of "numerical regularization" [30]. Numerical regularization is a technique for eliminating instabilities caused by the improper finite differencing of variables on or near the coordinate singularities in spherical polar or cylindrical coordinates. Unfortunately a straightforward application of this method does not work for the metric components for the simple reason that all of the metric functions are either quadratic (A , B , and D) or linear (C) in their angular behavior near $\theta = 0$. For standard finite difference operators, one can show that the angular finite differencing scheme of second order reproduces exactly the required (regular) result near the axis. Since spatial derivatives of the extrinsic curvature components are not present in the evolution equations with zero shift these have not been examined. Thornburg [50] has also examined irregularities along the symmetry axis and develops various regularization techniques that have not been tried in this code.

C. Convergence tests

The shift vector described in the previous section eliminates the axis instability only if the angular resolution is kept below about 50 zones. Once this limit is passed the code is once again unstable even if run with spherically symmetric initial data (as described above). However one can perform convergence tests for resolutions less than 50 angular zones and for these one gets satisfactory results, some of which are outlined in the next two sections. In this section we will give a prototypical example and compute the convergence rate for the evolution part of the code.

We compute the convergence rate for our evolution code by assuming the true value of some quantity Q_0 differs from the computed value Q via the formula

$$Q - Q_0 = k(\Delta\eta)^\sigma, \quad (78)$$

where k is some constant independent of the grid spacing or time step, $\Delta\eta$ is the radial grid spacing, and σ is the convergence rate. In practice this may not be strictly true, since k could have some dependence on grid and time step parameters, and $Q - Q_0$ is more generally a function of Δt and $\Delta\theta$. Furthermore the converge rate is likely to depend on the actual location of the quantity being measured, as different features develop locally in these calculations and boundaries may affect the convergence rate as well. Our calculations are performed with $\Delta\eta = \Delta\theta = \Delta t$ in all cases which makes the analysis more straightforward, but these effects can still complicate the convergence calculation.

With these caveats, if one assumes the error term has the form given by (78), then one may easily compute the convergence rate σ from the formula

$$\sigma = 1 + \frac{\partial \ln(Q')}{\partial \ln(\Delta\eta)}, \quad (79)$$

where $Q' = \partial Q / \partial \Delta\eta$. Using the above formulas, if we run the code at three different resolutions, we can compute the convergence rate σ for various quantities. As our initial data and time evolution schemes are formally second order (except for Brailovskaya, which is formally first order as noted in Sec. III A), we expect to obtain convergence exponents σ near 2 when second-order spatial derivatives are used. In practice we have computed convergence rates at different locations on the grid, with a number of different indicators, such as metric functions, extracted waveforms, apparent horizon masses, etc. The convergence results we report here were obtained with the leapfrog evolution scheme coupled with centered, second-order spatial derivatives.

Since it is the metric that is being evolved with this code, we report convergence rates based on comparisons of various metric functions. We find that generally the convergence exponent is near the expected value of 2. For example, we have run the code for three resolutions of (50×14) , (100×27) , and (200×53) zones and compared the radial metric function A at each resolution. For geodesic slicing, we obtain $\sigma = 2$ (to within about 1% over the entire grid), not just after a few time steps but even at late times in the evolution before the slicing hits the singularity at $t = \pi M$. This shows that the evolution equations in the code achieve second-order accuracy.

However, we point out that for maximal slicing the picture is more complicated, probably due to the fact that we must solve an elliptic equation for the lapse α , whose second derivatives are important in the evolution of the system. While the maximal slicing equation is coded in a second-order manner, formally one loses accuracy with each derivative of this solution. Therefore although α itself has a second-order numerical solution, spatial derivatives of α can be less than second order. We find that in the region of spacetime outside the peak that develops we achieve $\sigma \approx 2$, although inside this region the results are not consistent with this value. (The results can be greater than or less than 2, depending on the time slice on

which the convergence is computed.) We note that this is the region in which the lapse α has essentially frozen the evolution, and it is inside the horizon. Furthermore this is a gauge condition, so in principle this result does not affect physical results extracted from the simulations, such as waveforms and energies radiated. We find similar results for other metric functions and at other times, and conclude that our code is second-order accurate, at least in the region of spacetime where physical results are derived.

D. Evolution: Comparison with Schwarzschild

At late times, any energetically bound black hole spacetime with no net angular momentum should relax to a single Schwarzschild black hole. Multiple black holes will coalesce, and a distorted black hole will converge and eventually radiate higher multipole distortions away, leaving a spherical, single black hole spacetime. For these reasons, the single spherical black hole spacetime was studied in detail before moving on to the axisymmetric black hole spacetime considered here. The study of the spherical black hole spacetime provides a detailed test bed for the axisymmetric system. The axisymmetric black hole calculation must be able to reproduce the spherically symmetric results when given initial data which is spherically symmetric. Furthermore, at late times in the evolution of a distorted black hole the system again becomes Schwarzschild and again this spacetime must be accurately reproduced. Finally, the one-dimensional (1D) code provides us with the ability to run with large numbers of radial zones which would be impractical with the 2D code. In this way, we are able to see how many radial zones are required for accurate evolution of the longitudinal part of the gravitational field for a given length of time.

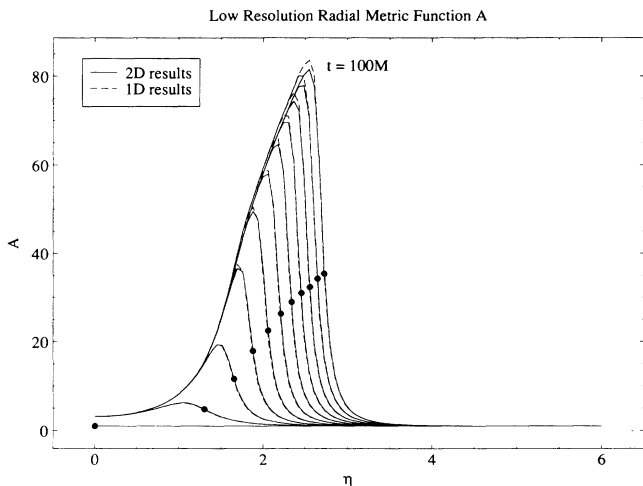


FIG. 3. We show the radial metric function A at intervals of $10M$ for both the 1D code (solid lines) and the 2D code (dashed lines). The position of the apparent horizon at each time is shown with a solid circle. The initial data set was the spherically symmetric black hole solution. 100 radial zones were used in both cases.

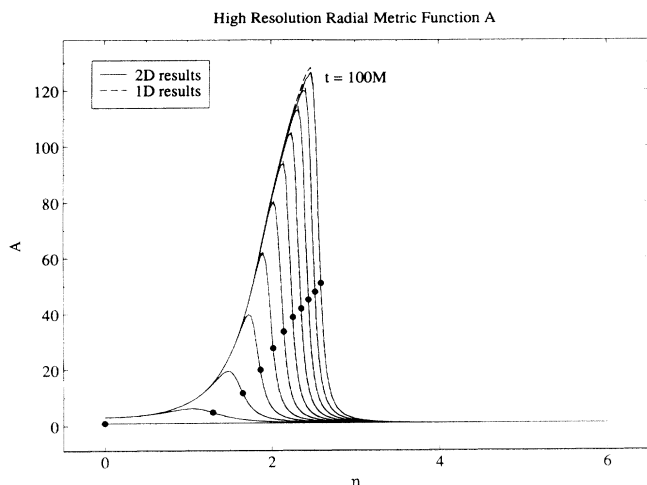


FIG. 4. We show the radial metric function A at intervals of $10M$ for both the 1D code (solid lines) and the 2D code (dashed lines). The position of the apparent horizon is shown with a solid circle. The initial data set was the spherically symmetric black hole solution. 200 radial zones were used in both cases.

When the amplitude of the gravitational wave is set to zero ($a = 0$) the solution to the initial-value problem is the Schwarzschild three-metric at $t = 0$. This initial data set can be evolved and checked against the equivalent results from the 1D code. Test results are presented in Figs. 3–6. These results all use the leapfrog evolution scheme with second-order spatial derivative approximations for both the 1D and 2D cases. In Figs. 3 and 4 we show the behavior of the radial metric function A on a number of different time slices for both the 1D and 2D codes, given spherically symmetric initial data. The solid lines show results from the 2D code, while dashed lines show results from the 1D code. The 2D results

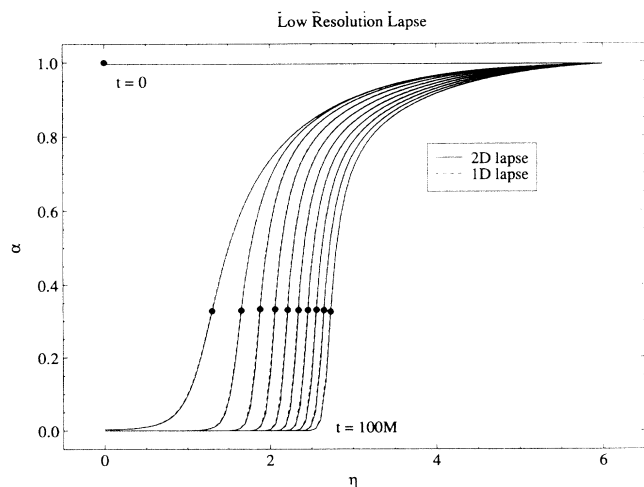


FIG. 5. We show the lapse function α at intervals of $10M$ for both the 1D code (solid lines) and the 2D code (dashed lines). The position of the apparent horizon is shown with a solid circle. 100 radial zones were used in both cases.

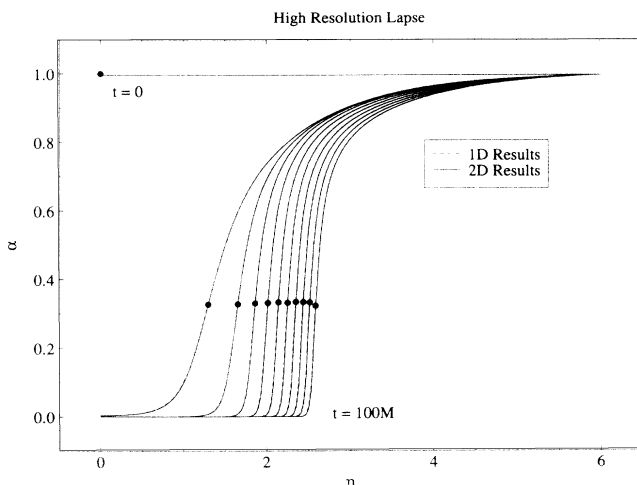


FIG. 6. We show the lapse function α at intervals of $10M$ for both the 1D code (solid lines) and the 2D code (dashed lines). The position of the apparent horizon is shown with a solid circle. 200 radial zones were used in both cases.

are taken along the equator ($\theta = \pi/2$). Other $\theta = \text{const}$ rays are virtually identical. Figure 3 shows results for 100 radial zones ($\Delta\eta = 0.06$), while Fig. 4 shows results for 200 radial zones ($\Delta\eta = 0.03$). Note that there is good agreement between the two codes at both high and low resolutions, although there are clear differences. Furthermore, the 2D data remain essentially spherically symmetric throughout the evolution, as it should (but see remarks below). In Figs. 5 and 6 we show the evolution of the maximal lapse function for the same runs. We have plotted the position of the apparent horizon on each line with a solid circle. The horizon has been located with an apparent horizon finder based on the method of Cook and York [17], described in detail in Refs. [3,19]. (A

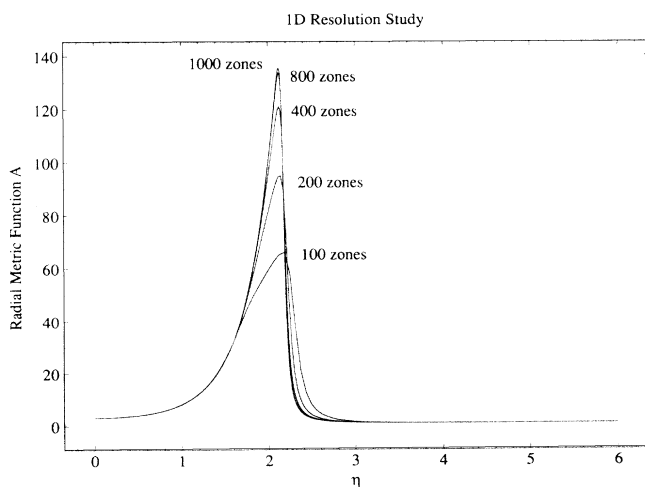


FIG. 7. We show the radial metric function A at various resolutions for the 1D code, from 100 radial zones ($\Delta\eta = 0.06$) to 1000 radial zones ($\Delta\eta = 0.006$). Each graph is taken at $t = 60M$. As the number of radial zones is increased toward 1000, the solution is converging to a very sharp peak.

full account of the dynamics of the apparent horizon for highly distorted black holes is given in Ref. [19].) Notice that the lapse quickly drops to very near zero inside the horizon, rising rapidly to a nearly constant value outside the horizon.

While there is good agreement between the 1D code and the 2D code at a given resolution, one can see that there is a noticeable difference between the results at the two different resolutions. There is agreement up to about $30M$, but afterward the low resolution cannot maintain the steepening profile present in the high resolution case. For comparison, a series of 1D runs for the radial metric function A at $60M$ are shown for different resolutions in Fig. 6. This work is detailed extensively in Refs. [5,14]. Here we provide it for reference so that one may see the resolution required for an accurate solution to the longitudinal part of the Einstein equations at late times (say, to $t = 100M$). Clearly, 200 radial zones is already unable to accurately resolve this peak by $60M$. Beyond this time the longitudinal part of the field loses accuracy, and this can be interpreted as a change in the mass of the system, as noted in Ref. [4].

For truly accurate longitudinal evolution through $t = 100M$, one can see that at least 1000 equally spaced radial zones are required, if second-order spatial differencing is used. Significantly more accurate results can be obtained if fourth-order spatial differencing is used, but, such a scheme breaks down when large gradients develop. We have experimented with fourth-order derivatives, and find that they work very well until gradients in the lapse and the radial metric function A become too large. The result is an instability, typically developing well before $100M$, depending on various computational parameters. A more sophisticated treatment allowing lower order derivatives in the region where large gradients develop might work, but has not yet been tried in our code.

The problems associated with the peak in the radial metric function A result from several factors. First, our choice of maximal time slicing causes very steep radial gradients in both the lapse function α and the radial metric function A . As these gradients increase during the evolution, the number of grid zones required to compute accurate derivatives of these functions also increases. Regardless of the number of grid zones present, at some time during the evolution the gradients will become steep enough that numerical derivatives will lose accuracy. An adaptive grid which would automatically add zones where required would be useful here, but we have not explored this technique yet. Another lapse can be chosen so that more gentle gradients are present. Bernstein [5] has studied many such algebraic slicing conditions that are similar in many ways to maximal slicing in the 1D case. Finally, an apparent horizon boundary condition that keeps the radial metric function A from growing can prevent this peak from developing altogether, but a full 2D implementation of this condition has yet to be fully developed [31,50].

We note that the 2D system evolved here is not truly spherical, although it appears very nearly so when analyzing different angular slices of the metric functions such

as $g_{\eta\eta}$. Our 2D gauge choice has not been altered for this test, so that both the β^η and β^θ components of the shift are present, as is the off diagonal component of the extrinsic curvature $K_{\eta\theta}$. These functions are not present in the 1D code, and in fact only the β^η shift is allowed in strict spherical symmetry. During the evolution these extra functions do remain small, although they do not vanish. They are required to maintain the stability of the evolution along the axis. If the shift is not used to maintain the diagonal three-metric condition, even spherical initial data will develop the axis instability, as described in Sec. IV B. However, when the shift is used to maintain this condition, the spherical evolution results of the 1D code can be very well reproduced with the 2D code.

E. Waveforms

Another major test of the code is provided by the dynamical evolution of a distorted black hole spacetime. As shown in Ref. [3] the initial data of the black hole plus gravitational wave spacetime can be chosen to produce a highly distorted black hole with smaller amplitudes producing smaller distortions. The evolution of the high amplitude data sets will be a major focus of future research. Provided that the amplitude of the initial wave is low enough, the spacetime should be accurately described by black hole perturbation theory. Such data sets have been considered in detail in Ref. [4] where perturbation theory was used to analyze the evolution. In that paper it was reported that our gauge choices and numerical methods result in a stable evolution, and in all cases studied the normal modes of the black hole were excited, dominating the late time gauge-invariant gravitational waveform. Careful comparisons were made to both the wavelength and damping time expected for a black hole of a given mass oscillating at its quasinormal mode frequency, and to the actual evolution of the linearized Einstein equations (the Zerilli equation [4]). The agreement between our code results and these tests was generally within a few percent, and small discrepancies arising from both code errors and physical, nonlinear effects were analyzed in detail. For a discussion of the physics of these calculations, we refer the interested reader to Ref. [4].

Here we provide a comparison of the various algorithms discussed in Sec. III above, and their effect on the waveforms extracted from the numerical evolution. In Sec. III we discussed three different methods used to evolve the Einstein equations forward in time, the leapfrog, Brailovskaya, and MacCormack methods. As shown in Ref. [14] all three of these methods performed well in spherical symmetry, although the Brailovskaya and MacCormack predictor-corrector methods had a slight advantage over leapfrog. However in the axisymmetric spacetimes, where gravitational waves are present, we find that the leapfrog method is best able to reproduce the known quasinormal mode frequencies of a perturbed black hole.

Figures 8(a) and 8(b) compare the $\ell = 2$ waveform extracted from the same low amplitude spacetime evolved with three different evolution schemes. The waveform is measured over a shell of proper area $4\pi(15M)^2$ [this

shell is located at $\eta = 3.4$ or about $r = 15m$, using (7), in the low amplitude spacetimes]. The methods are leapfrog, Brailovskaya, and MacCormack, each using second-order, centered spatial derivatives. Differences between the Brailovskaya and MacCormack method and the leapfrog method are then plotted, to bring out the differences between the methods. The leapfrog and MacCormack methods give similar results, but the Brailovskaya method clearly shows some widening and dissipation in the waveform at later times. This same effect has been noted in Ref. [41] in studies of self-gravitating scalar fields, and it can also be seen in simple studies of the flat-space scalar wave equation in 1D.

In Fig. 9 we show the waveform obtained with the leapfrog method plotted against a fit to the quasinormal modes of the black hole, known from perturbation theory [51]. This fit to the waveform is determined by ad-

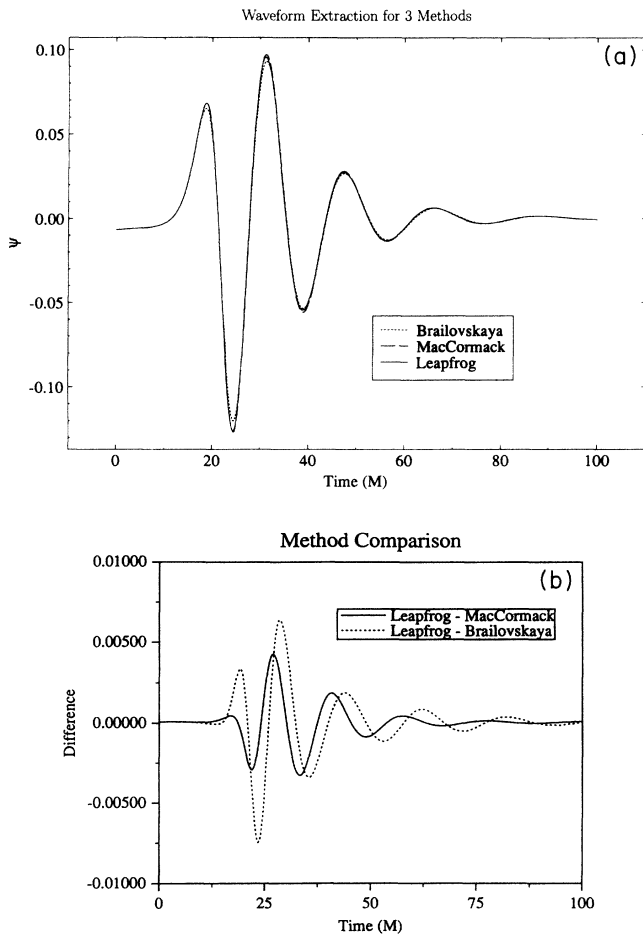


FIG. 8. (a) This figure shows the waveforms obtained for the spacetime (amplitude=0.1, range=0, width=1) measured over $r = 15m$ for the three evolution schemes. The grid resolution used was (200×53) . (b) This figure shows the differences in the $\ell = 2$ waveform for the same run. The leapfrog is the standard by which the other are measured. The difference between the leapfrog and the MacCormack is the solid line, and the difference between the leapfrog and the Brailovskaya is the dashed line. The leapfrog and MacCormack give similar results, while the Brailovskaya is more dispersive.

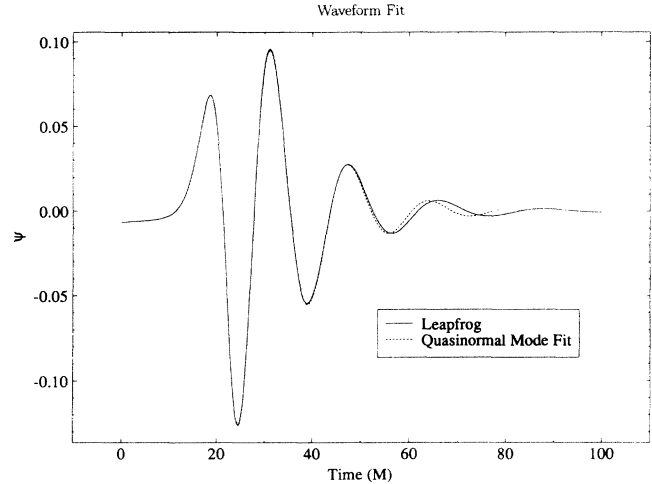


FIG. 9. This figure shows the $\ell = 2$ waveform against the least squares fit to the two lowest $\ell = 2$ quasinormal modes of the black hole for the leapfrog scheme from the last figure. The fit was done over the range $t = 25M$ to $t = 80M$. At late times the numerically computed waveform becomes slightly longer for reasons discussed in the text.

justing the phase and amplitude of the two lowest-lying (fundamental and first overtone) quasinormal modes for an $\ell = 2$ perturbation. The comparison is excellent except for the slight increase in wavelength at late times. This would be consistent with an apparent increase in mass of the hole which would be due to an error in computing the longitudinal part of the field. This error has been documented in Refs. [4,5] and has been discussed in Sec. III A. We know that the background is significantly more accurate if computed with the fourth-order spatial derivatives for t less than about $70M$. After this the fourth-order solutions become unstable and break down (at 200 radial zone resolution). We have also found that the waveform computed from the spacetime using the fourth-order spatial derivatives shows a smaller increase in wavelength at late times. This influence of the longitudinal part of the field on the waveform is also seen, and is stronger, in the $\ell = 4$ mode.

Figure 1 shows a comparison of the same waveform when the resolution is doubled in both the radial and angular directions. The $\ell = 2$ modes match up reasonably well for times less than about $t = 50M$ after which the low resolution signal shows a series of small growing oscillations. The same effect is seen more strongly in the $\ell = 4$ mode. An explanation for this is that the outgoing radiation is scattering off the increasingly coarse grid at large η ; some of the radiation is propagating inward from a region outside $r = 15m$ (about $\eta = 3.4$) and this is causing a signal at the $r = 15m$ detector. This has been confirmed by timing the arrival of the oscillations at different detectors in the spacetime. Recall (Sec. II E 1) that because of the increase in proper length of the zones there is a limit at which radiation will no longer propagate well on the grid. When a wave enters this region it is well known that some of it will be reflected back. From Fig. 1 it appears that the $r = 15M$ detector be-

gins to receive this radiation at about $t = 50M$ on the 100×27 grid. If the radiation initially is emitted near $r = 2M$ then this suggests that the backscattering location is in the neighborhood of $r = 34M$ or $\eta = 4.2$. At this location the number of grid points which would span a wave of wavelength $17M$ is about 9 on the 100×27 grid. This would indicate that in the number of zones per wavelength n discussed in Sec. II E 1 should be at least 10 at this grid spacing, $\Delta\eta = 0.06$. Using this figure we see that on the 200×53 grid the radiation will begin to backscatter near $r = 56m$ and so this radiation will not begin to affect the $r = 15m$ detector until about $t = 94M$, well after the calculation was stopped.

F. Energies

Another measure of the accuracy of the code is the consistency and conservation of various indicators of the mass of a black hole. The total ADM mass of the system can be written as [4]

$$M_{\text{ADM}} = -\frac{1}{2}\sqrt{2m} e^{\eta/2} \int_0^\pi \left(\frac{\partial\Psi}{\partial\eta} - \frac{\Psi}{2} \right) \sin\theta d\theta. \quad (80)$$

Note that in practice this quantity can only be computed at a finite radius (at the edge of our grid), and because we choose to make the conformal factor Ψ fixed in time, this quantity does not change with time. However it does give us the mass of the spacetime for comparison with other measures, such as the mass of the apparent horizon.

As described in Refs. [4,7] we have developed an apparent horizon finder and various methods for computing energy fluxes of gravitational waves emitted by the system, including integrating the Zerilli function ψ discussed in the previous section and the Newman-Penrose Weyl scalar Ψ_4 . These measures provide useful ways to check the accuracy of the code, as well as a means of extracting important physics from the simulations.

One useful quantity to monitor is the mass of the apparent horizon of the black hole as a function of time. For a dynamical black hole, we expect this mass function to increase as gravitational waves fall into the black hole, and then settle down to a value less than the ADM mass of the spacetime. This quantity has been reported in detail elsewhere [20], where it was shown that the apparent horizon mass increases and levels off to a level equal to the final mass of the black hole, but then begins to creep up rapidly at late times (after $t > 50M$) as the peak in the radial metric function becomes too steep to resolve accurately. The error in this sensitive measure of the black hole mass can exceed 50% at late times, depending on the resolution.

The measurements of the ADM mass and apparent horizon mass also provide a good ‘‘accounting’’ test of the code, as we can measure the energy leaving the black hole through some two-sphere outside the horizon. As the ADM mass represents the total mass of the spacetime, and the apparent horizon mass at late times (but before the artificial growth due to the effect discussed above) measures the final mass of the black hole, in prin-

ciple the energy flux of gravitational waves away from the black hole should make up the difference. Indeed, we are able to make these measurements with satisfactory results. For a typical simulation with run parameters $(a, \eta_0, w, n) = (1.5, 1.0, 1.0, 4)$, we find $M_{\text{ADM}} = 2.75$ is the total mass of the spacetime and $M_{\text{AH}} = 2.45$ is the approximate final mass of the black hole. As a check on the consistency of the final mass of the black hole we can perform a fit of known quasinormal waveforms, using the mass as a fitting parameter, to the extracted waveform obtained numerically. In this case we obtain a good fit for $M_{\text{hole}} = 2.5$, which is within a few percent of the horizon mass M_{AH} . Finally, we find that three different measures of the radiated energy, using the Zerilli function, the Newman-Penrose function Ψ_4 , and the Bel-Robinson Poynting vector [7] agree well with each other, producing a total energy output $E_{\text{rad}} = 0.22$. The overall accounting of the energies in the system is accurate to within less than 5%, and the largest uncertainty is in the final mass of the black hole. These figures are typical over a wide range of data sets.

V. SUMMARY AND FUTURE APPLICATIONS

We have presented a method for evolving axisymmetric black hole spacetimes with a numerical computer code. This code was built after extensive study of a spherically symmetric code designed to evolve the Schwarzschild geometry, and a number of comparisons have been made with results from that code. We have further tested the axisymmetric code for stability and accuracy under non-spherical conditions.

In a series of papers we will use this numerical code to explore the physics of axisymmetric black hole spacetimes, and as a tool to test results from 3D black hole codes now under development. Future applications of this code include (i) an extensive survey of possible candidates for tracking gravitational waves in both the linear and nonlinear regimes. This will include an analysis of the radiation extraction techniques developed by Abrahams and Evans to extract gravitational waves in the linear regime, as well as a number of nonlinear measures of gravitational waves, using the Newman-Penrose decomposition of the field, the Bel-Robinson tensor, the York tensor, and others. (ii) A detailed study of the dynamics of black hole apparent and event horizons (see, e.g., [20,52].) (iii) An exploration of the nonlinear collision of a gravitational wave with a single black hole. Here we will be interested in exploring in detail the nonlinear aspects of the interaction between black holes and gravitational waves. This will be a necessary step in the development of the project toward (iv) the collision of two black holes [19], and (v) full, 3D numerical relativity. We have also begun to consider (vi) rotating holes, that can be treated by modifying the present scheme to include the additional metric components required when rotation is present.

ACKNOWLEDGMENTS

We are pleased to acknowledge helpful discussion with many colleagues, most notably Peter Anninos, who helped develop extensions of the code described here, and Andrew Abrahams, Pete Anninos, Greg Cook, Joan Massó, and Wai-Mo Suen. The calculations presented in this paper were performed under a Grant from the National Center for Supercomputing Applications on the NCSA Cray Y-MP, Cray-2, Connection Machine models CM-2 and CM-5, and a Grant from the Pittsburgh Supercomputing Center on the Cray C-90. Additional funding for this project was provided by a Research Grant from the Natural Sciences and Engineering Research Council of Canada.

APPENDIX A: THE COMPLETE SET OF EINSTEIN EQUATIONS

This appendix presents the “3+1” form of the Einstein equations used in our code. All the equations are written *explicitly* in terms of the kinematic and dynamical variables and their partial derivatives with respect to the

spatial and temporal variables. The equations were derived from a package written in the MACSYMA language.

The most general three-metric for an axisymmetric nonrotating system is given by

$$\gamma_{ij} = \psi^4 \hat{\gamma}_{ij} = \begin{pmatrix} a\psi^4 & c\psi^4 & 0 \\ c\psi^4 & b\psi^4 & 0 \\ 0 & 0 & d\psi^4 \sin^2\theta \end{pmatrix}$$

and the most general extrinsic curvature tensor is

$$K_{ij} = \psi^4 \hat{K}_{ij} = \begin{pmatrix} H_a \psi^4 & H_c \psi^4 & 0 \\ H_c \psi^4 & H_b \psi^4 & 0 \\ 0 & 0 & H_d \psi^4 \sin^2\theta \end{pmatrix}.$$

The kinematic variables include the lapse function α and the shift vector with two nonzero components:

$$\beta^i = (\beta^\eta, \beta^\theta, 0).$$

With the addition of the notation

$$\delta = ab - c^2$$

the intrinsic Ricci curvature tensor for the three-dimensional spacelike hypersurfaces is determined from the three-metric and has the nonzero components

$$\begin{aligned} R_{\eta\eta} = & -\frac{2a^2 \frac{\partial\psi}{\partial\theta} \cot\theta}{\delta\psi} + \frac{2ac \frac{\partial\psi}{\partial\eta} \cot\theta}{\delta\psi} + \frac{a \frac{\partial c}{\partial\eta} \cot\theta}{\delta} - \frac{\frac{\partial a}{\partial\eta} c \cot\theta}{2\delta} - \frac{a \frac{\partial a}{\partial\theta} \cot\theta}{2\delta} - \frac{2a^2 \frac{\partial^2\psi}{\partial\theta^2}}{\delta\psi} \\ & - \frac{2a^2 \left(\frac{\partial\psi}{\partial\theta}\right)^2}{\delta\psi^2} + \frac{4ac \frac{\partial\psi}{\partial\eta} \frac{\partial\psi}{\partial\theta}}{\delta\psi^2} - \frac{a^2 \frac{\partial d}{\partial\theta} \frac{\partial\psi}{\partial\theta}}{\delta d\psi} + \frac{ac \frac{\partial d}{\partial\eta} \frac{\partial\psi}{\partial\theta}}{\delta d\psi} + \frac{2a \frac{\partial c}{\partial\eta} \frac{\partial\psi}{\partial\theta}}{\delta\psi} - \frac{\frac{\partial a}{\partial\eta} c \frac{\partial\psi}{\partial\theta}}{\delta\psi} \\ & - \frac{3a \frac{\partial a}{\partial\theta} \frac{\partial\psi}{\partial\theta}}{\delta\psi} - \frac{2a^2 c \frac{\partial c}{\partial\theta} \frac{\partial\psi}{\partial\theta}}{\delta^2\psi} + \frac{2a^2 b \frac{\partial c}{\partial\eta} \frac{\partial\psi}{\partial\theta}}{\delta^2\psi} - \frac{a^2 \frac{\partial b}{\partial\eta} c \frac{\partial\psi}{\partial\theta}}{\delta^2\psi} - \frac{a \frac{\partial a}{\partial\eta} b c \frac{\partial\psi}{\partial\theta}}{\delta^2\psi} + \frac{a^3 \frac{\partial b}{\partial\theta} \frac{\partial\psi}{\partial\theta}}{\delta^2\psi} \\ & + \frac{a^2 \frac{\partial a}{\partial\theta} b \frac{\partial\psi}{\partial\theta}}{\delta^2\psi} - \frac{2ab \frac{\partial^2\psi}{\partial\eta^2}}{\delta\psi} - \frac{2 \frac{\partial^2\psi}{\partial\eta^2}}{\psi} + \frac{4ac \frac{\partial^2\psi}{\partial\eta\partial\theta}}{\delta\psi} - \frac{2ab \left(\frac{\partial\psi}{\partial\eta}\right)^2}{\delta\psi^2} + \frac{6 \left(\frac{\partial\psi}{\partial\eta}\right)^2}{\psi^2} \\ & + \frac{ac \frac{\partial d}{\partial\theta} \frac{\partial\psi}{\partial\eta}}{\delta d\psi} - \frac{ab \frac{\partial d}{\partial\eta} \frac{\partial\psi}{\partial\eta}}{\delta d\psi} - \frac{2c \frac{\partial c}{\partial\eta} \frac{\partial\psi}{\partial\eta}}{\delta\psi} + \frac{\frac{\partial a}{\partial\theta} c \frac{\partial\psi}{\partial\eta}}{\delta\psi} - \frac{2a \frac{\partial b}{\partial\eta} \frac{\partial\psi}{\partial\eta}}{\delta\psi} + \frac{\frac{\partial a}{\partial\eta} b \frac{\partial\psi}{\partial\eta}}{\delta\psi} \\ & + \frac{2a^2 b \frac{\partial c}{\partial\theta} \frac{\partial\psi}{\partial\eta}}{\delta^2\psi} - \frac{2abc \frac{\partial c}{\partial\eta} \frac{\partial\psi}{\partial\eta}}{\delta^2\psi} - \frac{a^2 \frac{\partial b}{\partial\theta} c \frac{\partial\psi}{\partial\eta}}{\delta^2\psi} - \frac{a \frac{\partial a}{\partial\theta} b c \frac{\partial\psi}{\partial\eta}}{\delta^2\psi} + \frac{a^2 b \frac{\partial b}{\partial\eta} \frac{\partial\psi}{\partial\eta}}{\delta^2\psi} + \frac{a \frac{\partial a}{\partial\eta} b^2 \frac{\partial\psi}{\partial\eta}}{\delta^2\psi} \\ & + \frac{a \frac{\partial c}{\partial\eta} \frac{\partial d}{\partial\theta}}{2\delta d} - \frac{\frac{\partial a}{\partial\eta} c \frac{\partial d}{\partial\theta}}{4\delta d} - \frac{a \frac{\partial a}{\partial\theta} \frac{\partial d}{\partial\theta}}{4\delta d} - \frac{\frac{\partial^2 d}{\partial\eta^2}}{2d} + \frac{\left(\frac{\partial d}{\partial\eta}\right)^2}{4d^2} - \frac{c \frac{\partial c}{\partial\eta} \frac{\partial d}{\partial\eta}}{2\delta d} \\ & + \frac{\frac{\partial a}{\partial\theta} c \frac{\partial d}{\partial\eta}}{4\delta d} + \frac{\frac{\partial a}{\partial\eta} b \frac{\partial d}{\partial\eta}}{4\delta d} + \frac{a \frac{\partial^2 c}{\partial\eta\partial\theta}}{\delta} - \frac{a \frac{\partial^2 b}{\partial\eta^2}}{2\delta} - \frac{a \frac{\partial^2 a}{\partial\theta^2}}{2\delta} + \frac{ac \frac{\partial c}{\partial\eta} \frac{\partial c}{\partial\theta}}{\delta^2} \\ & - \frac{a \frac{\partial a}{\partial\theta} c \frac{\partial c}{\partial\theta}}{2\delta^2} - \frac{a \frac{\partial a}{\partial\eta} b \frac{\partial c}{\partial\theta}}{2\delta^2} - \frac{a \frac{\partial b}{\partial\eta} c \frac{\partial c}{\partial\theta}}{2\delta^2} - \frac{a^2 \frac{\partial b}{\partial\theta} \frac{\partial c}{\partial\eta}}{2\delta^2} + \frac{a \frac{\partial a}{\partial\eta} \frac{\partial b}{\partial\theta} c}{4\delta^2} - \frac{a \frac{\partial a}{\partial\theta} \frac{\partial b}{\partial\eta} c}{4\delta^2} \\ & + \frac{a^2 \frac{\partial a}{\partial\theta} \frac{\partial b}{\partial\theta}}{4\delta^2} + \frac{a^2 \left(\frac{\partial b}{\partial\eta}\right)^2}{4\delta^2} + \frac{a \frac{\partial a}{\partial\eta} b \frac{\partial b}{\partial\eta}}{4\delta^2} + \frac{a \left(\frac{\partial a}{\partial\theta}\right)^2 b}{4\delta^2}, \end{aligned}$$

$$\begin{aligned}
\frac{R_{\phi\phi}}{\sin^2\theta} = & -\frac{4ad\frac{\partial\psi}{\partial\theta}\cot\theta}{\delta\psi} + \frac{4cd\frac{\partial\psi}{\partial\eta}\cot\theta}{\delta\psi} - \frac{a\frac{\partial d}{\partial\theta}\cot\theta}{\delta} + \frac{c\frac{\partial d}{\partial\eta}\cot\theta}{\delta} - \frac{\frac{\partial a}{\partial\theta}d\cot\theta}{\delta} - \frac{ac\frac{\partial c}{\partial\theta}d\cot\theta}{\delta^2} \\
& + \frac{ab\frac{\partial c}{\partial\eta}d\cot\theta}{\delta^2} - \frac{a\frac{\partial b}{\partial\eta}cd\cot\theta}{2\delta^2} - \frac{\frac{\partial a}{\partial\eta}bcd\cot\theta}{2\delta^2} + \frac{a^2\frac{\partial b}{\partial\theta}d\cot\theta}{2\delta^2} + \frac{a\frac{\partial a}{\partial\theta}bd\cot\theta}{2\delta^2} - \frac{2ad\frac{\partial^2\psi}{\partial\theta^2}}{\delta\psi} \\
& - \frac{2ad\left(\frac{\partial\psi}{\partial\theta}\right)^2}{\delta\psi^2} + \frac{4cd\frac{\partial\psi}{\partial\eta}\frac{\partial\psi}{\partial\theta}}{\delta\psi^2} - \frac{2a\frac{\partial d}{\partial\theta}\frac{\partial\psi}{\partial\theta}}{\delta\psi} + \frac{2c\frac{\partial d}{\partial\eta}\frac{\partial\psi}{\partial\theta}}{\delta\psi} - \frac{2\frac{\partial a}{\partial\theta}d\frac{\partial\psi}{\partial\theta}}{\delta\psi} - \frac{2ac\frac{\partial c}{\partial\theta}d\frac{\partial\psi}{\partial\theta}}{\delta^2\psi} \\
& + \frac{2ab\frac{\partial c}{\partial\eta}d\frac{\partial\psi}{\partial\theta}}{\delta^2\psi} - \frac{a\frac{\partial b}{\partial\eta}cd\frac{\partial\psi}{\partial\theta}}{\delta^2\psi} - \frac{\frac{\partial a}{\partial\eta}bcd\frac{\partial\psi}{\partial\theta}}{\delta^2\psi} + \frac{a^2\frac{\partial b}{\partial\theta}d\frac{\partial\psi}{\partial\theta}}{\delta^2\psi} + \frac{a\frac{\partial a}{\partial\theta}bd\frac{\partial\psi}{\partial\theta}}{\delta^2\psi} - \frac{2bd\frac{\partial^2\psi}{\partial\eta^2}}{\delta\psi} \\
& + \frac{4cd\frac{\partial^2\psi}{\partial\eta\partial\theta}}{\delta\psi} - \frac{2bd\left(\frac{\partial\psi}{\partial\eta}\right)^2}{\delta\psi^2} + \frac{2c\frac{\partial d}{\partial\theta}\frac{\partial\psi}{\partial\eta}}{\delta\psi} - \frac{2b\frac{\partial d}{\partial\eta}\frac{\partial\psi}{\partial\eta}}{\delta\psi} - \frac{2\frac{\partial b}{\partial\eta}d\frac{\partial\psi}{\partial\eta}}{\delta\psi} + \frac{2ab\frac{\partial c}{\partial\theta}d\frac{\partial\psi}{\partial\eta}}{\delta^2\psi} \\
& - \frac{2bc\frac{\partial c}{\partial\eta}d\frac{\partial\psi}{\partial\eta}}{\delta^2\psi} - \frac{a\frac{\partial b}{\partial\theta}cd\frac{\partial\psi}{\partial\eta}}{\delta^2\psi} - \frac{\frac{\partial a}{\partial\theta}bcd\frac{\partial\psi}{\partial\eta}}{\delta^2\psi} + \frac{ab\frac{\partial b}{\partial\eta}d\frac{\partial\psi}{\partial\eta}}{\delta^2\psi} + \frac{\frac{\partial a}{\partial\eta}b^2d\frac{\partial\psi}{\partial\eta}}{\delta^2\psi} - \frac{a\frac{\partial^2d}{\partial\theta^2}}{2\delta} \\
& + \frac{a\left(\frac{\partial d}{\partial\theta}\right)^2}{4\delta d} - \frac{c\frac{\partial d}{\partial\eta}\frac{\partial d}{\partial\theta}}{2\delta d} - \frac{\frac{\partial a}{\partial\theta}\frac{\partial d}{\partial\theta}}{2\delta} - \frac{ac\frac{\partial c}{\partial\theta}\frac{\partial d}{\partial\theta}}{2\delta^2} + \frac{ab\frac{\partial c}{\partial\eta}\frac{\partial d}{\partial\theta}}{2\delta^2} - \frac{a\frac{\partial b}{\partial\eta}c\frac{\partial d}{\partial\theta}}{4\delta^2} \\
& - \frac{\frac{\partial a}{\partial\eta}bc\frac{\partial d}{\partial\theta}}{4\delta^2} + \frac{a^2\frac{\partial b}{\partial\theta}\frac{\partial d}{\partial\theta}}{4\delta^2} + \frac{a\frac{\partial a}{\partial\theta}b\frac{\partial d}{\partial\theta}}{4\delta^2} - \frac{b\frac{\partial^2d}{\partial\eta^2}}{2\delta} + \frac{c\frac{\partial^2d}{\partial\eta\partial\theta}}{\delta} + \frac{b\left(\frac{\partial d}{\partial\eta}\right)^2}{4\delta d} \\
& - \frac{\frac{\partial b}{\partial\eta}\frac{\partial d}{\partial\eta}}{2\delta} + \frac{ab\frac{\partial c}{\partial\theta}\frac{\partial d}{\partial\eta}}{2\delta^2} - \frac{bc\frac{\partial c}{\partial\eta}\frac{\partial d}{\partial\eta}}{2\delta^2} - \frac{a\frac{\partial b}{\partial\theta}c\frac{\partial d}{\partial\eta}}{4\delta^2} - \frac{\frac{\partial a}{\partial\theta}bc\frac{\partial d}{\partial\eta}}{4\delta^2} + \frac{ab\frac{\partial b}{\partial\eta}\frac{\partial d}{\partial\eta}}{4\delta^2} + \frac{\frac{\partial a}{\partial\eta}b^2\frac{\partial d}{\partial\eta}}{4\delta^2} + \frac{ad}{\delta}.
\end{aligned}$$

The Hamiltonian constraint written explicitly in terms of the extrinsic and intrinsic curvature components is

$$0 = \frac{R_{\phi\phi}}{d\psi^4\sin^2\theta} - \frac{2R_{\eta\theta}c}{\delta\psi^4} + \frac{R_{\eta\eta}a}{\delta\psi^4} + \frac{R_{\theta\theta}b}{\delta\psi^4} - \frac{2H_c^2}{\delta} - \frac{4cH_dH_c}{\delta d} + \frac{2H_aH_b}{\delta} + \frac{2aH_dH_b}{\delta d} + \frac{2bH_dH_a}{\delta d}.$$

Explicitly evaluating the curvature scalar R of the 3D hypersurfaces yields

$$\begin{aligned}
0 = & -\frac{8a\frac{\partial\psi}{\partial\theta}\cot\theta}{\delta\psi^5} + \frac{8c\frac{\partial\psi}{\partial\eta}\cot\theta}{\delta\psi^5} - \frac{2a\frac{\partial d}{\partial\theta}\cot\theta}{\delta d\psi^4} + \frac{2c\frac{\partial d}{\partial\eta}\cot\theta}{\delta d\psi^4} - \frac{2\frac{\partial a}{\partial\theta}\cot\theta}{\delta\psi^4} \\
& - \frac{2ac\frac{\partial c}{\partial\theta}\cot\theta}{\delta^2\psi^4} + \frac{2ab\frac{\partial c}{\partial\eta}\cot\theta}{\delta^2\psi^4} - \frac{a\frac{\partial b}{\partial\eta}c\cot\theta}{\delta^2\psi^4} - \frac{\frac{\partial a}{\partial\eta}bc\cot\theta}{\delta^2\psi^4} + \frac{a^2\frac{\partial b}{\partial\theta}\cot\theta}{\delta^2\psi^4} + \frac{a\frac{\partial a}{\partial\theta}b\cot\theta}{\delta^2\psi^4} \\
& - \frac{8a\frac{\partial^2\psi}{\partial\theta^2}}{\delta\psi^5} - \frac{4a\frac{\partial d}{\partial\theta}\frac{\partial\psi}{\partial\theta}}{\delta d\psi^5} + \frac{4c\frac{\partial d}{\partial\eta}\frac{\partial\psi}{\partial\theta}}{\delta d\psi^5} - \frac{8\frac{\partial a}{\partial\theta}\frac{\partial\psi}{\partial\theta}}{\delta\psi^5} - \frac{8ac\frac{\partial c}{\partial\theta}\frac{\partial\psi}{\partial\theta}}{\delta^2\psi^5} + \frac{8ab\frac{\partial c}{\partial\eta}\frac{\partial\psi}{\partial\theta}}{\delta^2\psi^5} \\
& - \frac{4a\frac{\partial b}{\partial\eta}c\frac{\partial\psi}{\partial\theta}}{\delta^2\psi^5} - \frac{4\frac{\partial a}{\partial\eta}bc\frac{\partial\psi}{\partial\theta}}{\delta^2\psi^5} + \frac{4a^2\frac{\partial b}{\partial\theta}\frac{\partial\psi}{\partial\theta}}{\delta^2\psi^5} + \frac{4a\frac{\partial a}{\partial\theta}b\frac{\partial\psi}{\partial\theta}}{\delta^2\psi^5} - \frac{8b\frac{\partial^2\psi}{\partial\eta^2}}{\delta\psi^5} + \frac{16c\frac{\partial^2\psi}{\partial\eta\partial\theta}}{\delta\psi^5} \\
& + \frac{4c\frac{\partial d}{\partial\theta}\frac{\partial\psi}{\partial\eta}}{\delta d\psi^5} - \frac{4b\frac{\partial d}{\partial\eta}\frac{\partial\psi}{\partial\eta}}{\delta d\psi^5} - \frac{8\frac{\partial b}{\partial\eta}\frac{\partial\psi}{\partial\eta}}{\delta\psi^5} + \frac{8ab\frac{\partial c}{\partial\theta}\frac{\partial\psi}{\partial\eta}}{\delta^2\psi^5} - \frac{8bc\frac{\partial c}{\partial\eta}\frac{\partial\psi}{\partial\eta}}{\delta^2\psi^5} - \frac{4a\frac{\partial b}{\partial\theta}c\frac{\partial\psi}{\partial\eta}}{\delta^2\psi^5} \\
& - \frac{4\frac{\partial a}{\partial\theta}bc\frac{\partial\psi}{\partial\eta}}{\delta^2\psi^5} + \frac{4ab\frac{\partial b}{\partial\eta}\frac{\partial\psi}{\partial\eta}}{\delta^2\psi^5} + \frac{4\frac{\partial a}{\partial\eta}b^2\frac{\partial\psi}{\partial\eta}}{\delta^2\psi^5} - \frac{a\frac{\partial^2d}{\partial\theta^2}}{\delta d\psi^4} + \frac{a\left(\frac{\partial d}{\partial\theta}\right)^2}{2\delta d^2\psi^4} - \frac{c\frac{\partial d}{\partial\eta}\frac{\partial d}{\partial\theta}}{\delta d^2\psi^4} \\
& - \frac{\frac{\partial a}{\partial\theta}\frac{\partial d}{\partial\theta}}{\delta d\psi^4} - \frac{ac\frac{\partial c}{\partial\theta}\frac{\partial d}{\partial\theta}}{\delta^2d\psi^4} + \frac{ab\frac{\partial c}{\partial\eta}\frac{\partial d}{\partial\theta}}{\delta^2d\psi^4} - \frac{a\frac{\partial b}{\partial\eta}c\frac{\partial d}{\partial\theta}}{2\delta^2d\psi^4} - \frac{\frac{\partial a}{\partial\eta}bc\frac{\partial d}{\partial\theta}}{2\delta^2d\psi^4} + \frac{a^2\frac{\partial b}{\partial\theta}\frac{\partial d}{\partial\theta}}{2\delta^2d\psi^4} \\
& + \frac{a\frac{\partial a}{\partial\theta}b\frac{\partial d}{\partial\theta}}{2\delta^2d\psi^4} - \frac{b\frac{\partial^2d}{\partial\eta^2}}{\delta d\psi^4} + \frac{2c\frac{\partial^2d}{\partial\eta\partial\theta}}{\delta d\psi^4} + \frac{b\left(\frac{\partial d}{\partial\eta}\right)^2}{2\delta d^2\psi^4} - \frac{\frac{\partial b}{\partial\eta}\frac{\partial d}{\partial\eta}}{\delta d\psi^4} + \frac{ab\frac{\partial c}{\partial\theta}\frac{\partial d}{\partial\eta}}{\delta^2d\psi^4} \\
& - \frac{bc\frac{\partial c}{\partial\eta}\frac{\partial d}{\partial\eta}}{\delta^2d\psi^4} - \frac{a\frac{\partial b}{\partial\theta}c\frac{\partial d}{\partial\eta}}{2\delta^2d\psi^4} - \frac{\frac{\partial a}{\partial\theta}bc\frac{\partial d}{\partial\eta}}{2\delta^2d\psi^4} + \frac{ab\frac{\partial b}{\partial\eta}\frac{\partial d}{\partial\eta}}{2\delta^2d\psi^4} + \frac{\frac{\partial a}{\partial\eta}b^2\frac{\partial d}{\partial\eta}}{2\delta^2d\psi^4} + \frac{2\frac{\partial^2c}{\partial\eta\partial\theta}}{\delta\psi^4} \\
& - \frac{\frac{\partial^2b}{\partial\eta^2}}{\delta\psi^4} - \frac{\frac{\partial^2a}{\partial\theta^2}}{\delta\psi^4} + \frac{2a}{\delta\psi^4} + \frac{2c\frac{\partial c}{\partial\eta}\frac{\partial c}{\partial\theta}}{\delta^2\psi^4} - \frac{\frac{\partial a}{\partial\theta}c\frac{\partial c}{\partial\theta}}{\delta^2\psi^4} - \frac{\frac{\partial a}{\partial\eta}b\frac{\partial c}{\partial\theta}}{\delta^2\psi^4} \\
& - \frac{\frac{\partial b}{\partial\eta}c\frac{\partial c}{\partial\eta}}{\delta^2\psi^4} - \frac{a\frac{\partial b}{\partial\theta}\frac{\partial c}{\partial\eta}}{\delta^2\psi^4} + \frac{\frac{\partial a}{\partial\eta}\frac{\partial b}{\partial\theta}c}{2\delta^2\psi^4} - \frac{\frac{\partial a}{\partial\theta}\frac{\partial b}{\partial\eta}c}{2\delta^2\psi^4} + \frac{a\frac{\partial a}{\partial\theta}\frac{\partial b}{\partial\theta}}{2\delta^2\psi^4} + \frac{a\left(\frac{\partial b}{\partial\eta}\right)^2}{2\delta^2\psi^4} \\
& + \frac{\frac{\partial a}{\partial\eta}b\frac{\partial b}{\partial\eta}}{2\delta^2\psi^4} + \frac{\left(\frac{\partial a}{\partial\theta}\right)^2b}{2\delta^2\psi^4} - \frac{2H_c^2}{\delta} - \frac{4cH_dH_c}{\delta d} + \frac{2H_aH_b}{\delta} + \frac{2aH_dH_b}{\delta d} + \frac{2bH_dH_a}{\delta d}
\end{aligned}$$

and the two components of the momentum constraint become, for $H_1 = 0$,

$$\begin{aligned}
0 = & + \frac{a H_c \cot \theta}{\delta} - \frac{c H_a \cot \theta}{\delta} + \frac{4 c H_c \frac{\partial \psi}{\partial \theta}}{\delta \psi} + \frac{14 a H_c \frac{\partial \psi}{\partial \theta}}{\delta \psi} - \frac{8 a b c H_c \frac{\partial \psi}{\partial \theta}}{\delta^2 \psi} \\
& - \frac{8 a^2 b H_c \frac{\partial \psi}{\partial \theta}}{\delta^2 \psi} - \frac{4 a H_b \frac{\partial \psi}{\partial \theta}}{\delta \psi} + \frac{2 a^2 c H_b \frac{\partial \psi}{\partial \theta}}{\delta^2 \psi} + \frac{4 a^2 b H_b \frac{\partial \psi}{\partial \theta}}{\delta^2 \psi} - \frac{10 c H_a \frac{\partial \psi}{\partial \theta}}{\delta \psi} - \frac{4 b H_a \frac{\partial \psi}{\partial \theta}}{\delta \psi} \\
& + \frac{6 a b c H_a \frac{\partial \psi}{\partial \theta}}{\delta^2 \psi} + \frac{4 a b^2 H_a \frac{\partial \psi}{\partial \theta}}{\delta^2 \psi} - \frac{2 c H_c \frac{\partial \psi}{\partial \eta}}{\delta \psi} - \frac{8 b H_c \frac{\partial \psi}{\partial \eta}}{\delta \psi} + \frac{8 a b^2 H_c \frac{\partial \psi}{\partial \eta}}{\delta^2 \psi} + \frac{4 c H_b \frac{\partial \psi}{\partial \eta}}{\delta \psi} \\
& - \frac{4 a H_b \frac{\partial \psi}{\partial \eta}}{\delta \psi} - \frac{4 a b c H_b \frac{\partial \psi}{\partial \eta}}{\delta^2 \psi} + \frac{2 a^2 b H_b \frac{\partial \psi}{\partial \eta}}{\delta^2 \psi} + \frac{6 b H_a \frac{\partial \psi}{\partial \eta}}{\delta \psi} - \frac{4 b^2 c H_a \frac{\partial \psi}{\partial \eta}}{\delta^2 \psi} - \frac{2 a b^2 H_a \frac{\partial \psi}{\partial \eta}}{\delta^2 \psi} \\
& - \frac{2 H_d \frac{\partial \psi}{\partial \eta}}{d \psi} - \frac{c \frac{\partial H_c}{\partial \theta}}{\delta} - \frac{a \frac{\partial H_c}{\partial \theta}}{\delta} + \frac{2 a b c \frac{\partial H_c}{\partial \theta}}{\delta^2} + \frac{2 a^2 b \frac{\partial H_c}{\partial \theta}}{\delta^2} + \frac{2 c \frac{\partial H_c}{\partial \eta}}{\delta} \\
& + \frac{2 b \frac{\partial H_c}{\partial \eta}}{\delta} - \frac{2 a b c \frac{\partial H_c}{\partial \eta}}{\delta^2} - \frac{2 a b^2 \frac{\partial H_c}{\partial \eta}}{\delta^2} + \frac{a \frac{\partial d}{\partial \theta} H_c}{2 \delta d} - \frac{c \frac{\partial d}{\partial \eta} H_c}{2 \delta d} + \frac{2 \frac{\partial c}{\partial \theta} H_c}{\delta} \\
& - \frac{2 \frac{\partial c}{\partial \eta} H_c}{\delta} + \frac{2 \frac{\partial b}{\partial \eta} H_c}{\delta} - \frac{\frac{\partial a}{\partial \theta} H_c}{\delta} - \frac{5 a c \frac{\partial c}{\partial \theta} H_c}{\delta^2} - \frac{10 a b \frac{\partial c}{\partial \theta} H_c}{\delta^2} + \frac{6 b c \frac{\partial c}{\partial \eta} H_c}{\delta^2} \\
& + \frac{3 a \frac{\partial b}{\partial \theta} c H_c}{\delta^2} - \frac{2 a \frac{\partial b}{\partial \eta} c H_c}{\delta^2} + \frac{3 \frac{\partial a}{\partial \theta} b c H_c}{\delta^2} - \frac{2 \frac{\partial a}{\partial \eta} b c H_c}{\delta^2} + \frac{7 a^2 \frac{\partial b}{\partial \theta} H_c}{2 \delta^2} \\
& - \frac{6 a b \frac{\partial b}{\partial \eta} H_c}{\delta^2} - \frac{4 \frac{\partial a}{\partial \eta} b^2 H_c}{\delta^2} + \frac{11 a \frac{\partial a}{\partial \theta} b H_c}{2 \delta^2} + \frac{8 a^2 b c \frac{\partial c}{\partial \theta} H_c}{\delta^3} + \frac{8 a^2 b^2 \frac{\partial c}{\partial \theta} H_c}{\delta^3} - \frac{8 a b^2 c \frac{\partial c}{\partial \eta} H_c}{\delta^3} \\
& - \frac{4 a^2 b^2 \frac{\partial c}{\partial \eta} H_c}{\delta^3} - \frac{4 a^2 b \frac{\partial b}{\partial \theta} c H_c}{\delta^3} + \frac{2 a^2 b \frac{\partial b}{\partial \eta} c H_c}{\delta^3} - \frac{4 a \frac{\partial a}{\partial \theta} b^2 c H_c}{\delta^3} + \frac{2 a \frac{\partial a}{\partial \eta} b^2 c H_c}{\delta^3} - \frac{4 a^3 b \frac{\partial b}{\partial \theta} H_c}{\delta^3} \\
& + \frac{4 a^2 b^2 \frac{\partial b}{\partial \eta} H_c}{\delta^3} + \frac{4 a \frac{\partial a}{\partial \eta} b^3 H_c}{\delta^3} - \frac{4 a^2 \frac{\partial a}{\partial \theta} b^2 H_c}{\delta^3} + \frac{a \frac{\partial H_b}{\partial \theta}}{\delta} - \frac{a^2 c \frac{\partial H_b}{\partial \theta}}{\delta^2} - \frac{a^2 b \frac{\partial H_b}{\partial \theta}}{\delta^2} \\
& - \frac{c \frac{\partial H_b}{\partial \eta}}{\delta} - \frac{2 a \frac{\partial H_b}{\partial \eta}}{\delta} + \frac{a b c \frac{\partial H_b}{\partial \eta}}{\delta^2} + \frac{a^2 b \frac{\partial H_b}{\partial \eta}}{\delta^2} + \frac{2 \frac{\partial c}{\partial \eta} H_b}{\delta} + \frac{\frac{\partial a}{\partial \theta} H_b}{\delta} \\
& - \frac{\frac{\partial a}{\partial \eta} H_b}{\delta} + \frac{3 a c \frac{\partial c}{\partial \theta} H_b}{\delta^2} + \frac{4 a^2 \frac{\partial c}{\partial \theta} H_b}{\delta^2} - \frac{2 a c \frac{\partial c}{\partial \eta} H_b}{\delta^2} - \frac{6 a b \frac{\partial c}{\partial \eta} H_b}{\delta^2} + \frac{2 a \frac{\partial b}{\partial \eta} c H_b}{\delta^2} \\
& + \frac{2 \frac{\partial a}{\partial \eta} b c H_b}{\delta^2} - \frac{5 a \frac{\partial a}{\partial \theta} c H_b}{2 \delta^2} - \frac{2 a^2 \frac{\partial b}{\partial \theta} H_b}{\delta^2} + \frac{3 a^2 \frac{\partial b}{\partial \eta} H_b}{2 \delta^2} - \frac{3 a \frac{\partial a}{\partial \theta} b H_b}{\delta^2} + \frac{2 a \frac{\partial a}{\partial \eta} b H_b}{\delta^2} \\
& - \frac{4 a^2 b c \frac{\partial c}{\partial \theta} H_b}{\delta^3} - \frac{4 a^3 b \frac{\partial c}{\partial \theta} H_b}{\delta^3} + \frac{2 a^2 b c \frac{\partial c}{\partial \eta} H_b}{\delta^3} + \frac{4 a^2 b^2 \frac{\partial c}{\partial \eta} H_b}{\delta^3} + \frac{2 a^3 \frac{\partial b}{\partial \theta} c H_b}{\delta^3} - \frac{2 a^2 b \frac{\partial b}{\partial \theta} c H_b}{\delta^3} \\
& - \frac{2 a \frac{\partial a}{\partial \eta} b^2 c H_b}{\delta^3} + \frac{2 a^2 \frac{\partial a}{\partial \theta} b c H_b}{\delta^3} + \frac{2 a^3 b \frac{\partial b}{\partial \theta} H_b}{\delta^3} - \frac{a^3 b \frac{\partial b}{\partial \eta} H_b}{\delta^3} + \frac{2 a^2 \frac{\partial a}{\partial \theta} b^2 H_b}{\delta^3} - \frac{a^2 \frac{\partial a}{\partial \eta} b^2 H_b}{\delta^3} \\
& + \frac{b \frac{\partial H_a}{\partial \theta}}{\delta} - \frac{a b c \frac{\partial H_a}{\partial \theta}}{\delta^2} - \frac{a b^2 \frac{\partial H_a}{\partial \theta}}{\delta^2} - \frac{b \frac{\partial H_a}{\partial \eta}}{\delta} + \frac{b^2 c \frac{\partial H_a}{\partial \eta}}{\delta^2} + \frac{a b^2 \frac{\partial H_a}{\partial \eta}}{\delta^2} \\
& - \frac{c \frac{\partial d}{\partial \theta} H_a}{2 \delta d} + \frac{b \frac{\partial d}{\partial \eta} H_a}{2 \delta d} - \frac{2 \frac{\partial c}{\partial \theta} H_a}{\delta} + \frac{\frac{\partial b}{\partial \theta} H_a}{\delta} + \frac{3 b c \frac{\partial c}{\partial \theta} H_a}{\delta^2} + \frac{5 a b \frac{\partial c}{\partial \theta} H_a}{\delta^2} \\
& - \frac{2 b c \frac{\partial c}{\partial \eta} H_a}{\delta^2} - \frac{4 b^2 \frac{\partial c}{\partial \eta} H_a}{\delta^2} - \frac{3 a \frac{\partial b}{\partial \theta} c H_a}{2 \delta^2} + \frac{2 b \frac{\partial b}{\partial \eta} c H_a}{\delta^2} - \frac{\frac{\partial a}{\partial \theta} b c H_a}{\delta^2} - \frac{3 a b \frac{\partial b}{\partial \theta} H_a}{\delta^2} \\
& + \frac{3 a b \frac{\partial b}{\partial \eta} H_a}{2 \delta^2} - \frac{2 \frac{\partial a}{\partial \theta} b^2 H_a}{\delta^2} + \frac{\frac{\partial a}{\partial \eta} b^2 H_a}{\delta^2} - \frac{4 a b^2 c \frac{\partial c}{\partial \theta} H_a}{\delta^3} - \frac{4 a^2 b^2 \frac{\partial c}{\partial \theta} H_a}{\delta^3} + \frac{2 a b^2 c \frac{\partial c}{\partial \eta} H_a}{\delta^3} \\
& + \frac{4 a b^3 \frac{\partial c}{\partial \eta} H_a}{\delta^3} + \frac{2 a^2 b \frac{\partial b}{\partial \theta} c H_a}{\delta^3} - \frac{2 a b^2 \frac{\partial b}{\partial \eta} c H_a}{\delta^3} - \frac{2 \frac{\partial a}{\partial \eta} b^3 c H_a}{\delta^3} + \frac{2 a \frac{\partial a}{\partial \theta} b^2 c H_a}{\delta^3} + \frac{2 a^2 b^2 \frac{\partial b}{\partial \theta} H_a}{\delta^3} \\
& - \frac{a^2 b^2 \frac{\partial b}{\partial \eta} H_a}{\delta^3} + \frac{2 a \frac{\partial a}{\partial \theta} b^3 H_a}{\delta^3} - \frac{a \frac{\partial a}{\partial \eta} b^3 H_a}{\delta^3} - \frac{\frac{\partial H_d}{\partial \eta}}{d} + \frac{\frac{\partial d}{\partial \eta} H_d}{2 d^2}
\end{aligned}$$

and, for $H_2 = 0$,

$$\begin{aligned}
0 = & -\frac{c H_c \cot \theta}{\delta} + \frac{a H_b \cot \theta}{\delta} - \frac{H_d \cot \theta}{d} - \frac{6 c H_c \frac{\partial \psi}{\partial \theta}}{\delta \psi} - \frac{8 a H_c \frac{\partial \psi}{\partial \theta}}{\delta \psi} \\
& + \frac{8 a b c H_c \frac{\partial \psi}{\partial \theta}}{\delta^2 \psi} + \frac{8 a^2 b H_c \frac{\partial \psi}{\partial \theta}}{\delta^2 \psi} + \frac{8 a H_b \frac{\partial \psi}{\partial \theta}}{\delta \psi} - \frac{4 a^2 c H_b \frac{\partial \psi}{\partial \theta}}{\delta^2 \psi} - \frac{6 a^2 b H_b \frac{\partial \psi}{\partial \theta}}{\delta^2 \psi} + \frac{4 c H_a \frac{\partial \psi}{\partial \theta}}{\delta \psi} \\
& + \frac{2 b H_a \frac{\partial \psi}{\partial \theta}}{\delta \psi} - \frac{4 a b c H_a \frac{\partial \psi}{\partial \theta}}{\delta^2 \psi} - \frac{2 a b^2 H_a \frac{\partial \psi}{\partial \theta}}{\delta^2 \psi} - \frac{2 H_d \frac{\partial \psi}{\partial \theta}}{d \psi} + \frac{4 c H_c \frac{\partial \psi}{\partial \eta}}{\delta \psi} + \frac{18 b H_c \frac{\partial \psi}{\partial \eta}}{\delta \psi} \\
& - \frac{8 a b c H_c \frac{\partial \psi}{\partial \eta}}{\delta^2 \psi} - \frac{16 a b^2 H_c \frac{\partial \psi}{\partial \eta}}{\delta^2 \psi} - \frac{10 c H_b \frac{\partial \psi}{\partial \eta}}{\delta \psi} - \frac{4 a H_b \frac{\partial \psi}{\partial \eta}}{\delta \psi} + \frac{10 a b c H_b \frac{\partial \psi}{\partial \eta}}{\delta^2 \psi} + \frac{4 a^2 b H_b \frac{\partial \psi}{\partial \eta}}{\delta^2 \psi} \\
& - \frac{4 b H_a \frac{\partial \psi}{\partial \eta}}{\delta \psi} + \frac{6 b^2 c H_a \frac{\partial \psi}{\partial \eta}}{\delta^2 \psi} + \frac{4 a b^2 H_a \frac{\partial \psi}{\partial \eta}}{\delta^2 \psi} + \frac{2 c \frac{\partial H_c}{\partial \theta}}{\delta} + \frac{2 a \frac{\partial H_c}{\partial \theta}}{\delta} - \frac{2 a b c \frac{\partial H_c}{\partial \theta}}{\delta^2} \\
& - \frac{2 a^2 b \frac{\partial H_c}{\partial \theta}}{\delta^2} - \frac{c \frac{\partial H_c}{\partial \eta}}{\delta} - \frac{b \frac{\partial H_c}{\partial \eta}}{\delta} + \frac{2 a b c \frac{\partial H_c}{\partial \eta}}{\delta^2} + \frac{2 a b^2 \frac{\partial H_c}{\partial \eta}}{\delta^2} - \frac{c \frac{\partial d}{\partial \theta} H_c}{2 \delta d} \\
& + \frac{b \frac{\partial d}{\partial \eta} H_c}{2 \delta d} - \frac{3 \frac{\partial c}{\partial \theta} H_c}{\delta} + \frac{2 \frac{\partial c}{\partial \eta} H_c}{\delta} - \frac{\frac{\partial b}{\partial \eta} H_c}{\delta} + \frac{2 \frac{\partial a}{\partial \theta} H_c}{\delta} + \frac{6 a c \frac{\partial c}{\partial \theta} H_c}{\delta^2} \\
& + \frac{11 a b \frac{\partial c}{\partial \theta} H_c}{\delta^2} - \frac{6 b c \frac{\partial c}{\partial \eta} H_c}{\delta^2} - \frac{10 a b \frac{\partial c}{\partial \eta} H_c}{\delta^2} - \frac{7 a \frac{\partial b}{\partial \theta} c H_c}{2 \delta^2} + \frac{3 a \frac{\partial b}{\partial \eta} c H_c}{\delta^2} - \frac{7 \frac{\partial a}{\partial \theta} b c H_c}{2 \delta^2} \\
& + \frac{3 \frac{\partial a}{\partial \eta} b c H_c}{\delta^2} - \frac{4 a^2 \frac{\partial b}{\partial \theta} H_c}{\delta^2} + \frac{7 a b \frac{\partial b}{\partial \eta} H_c}{\delta^2} + \frac{5 \frac{\partial a}{\partial \eta} b^2 H_c}{\delta^2} - \frac{6 a \frac{\partial a}{\partial \theta} b H_c}{\delta^2} - \frac{8 a^2 b c \frac{\partial c}{\partial \theta} H_c}{\delta^3} \\
& - \frac{8 a^2 b^2 \frac{\partial c}{\partial \theta} H_c}{\delta^3} + \frac{12 a b^2 c \frac{\partial c}{\partial \eta} H_c}{\delta^3} + \frac{8 a^2 b^2 \frac{\partial c}{\partial \eta} H_c}{\delta^3} + \frac{4 a^2 b \frac{\partial b}{\partial \theta} c H_c}{\delta^3} - \frac{4 a^2 b \frac{\partial b}{\partial \eta} c H_c}{\delta^3} + \frac{4 a \frac{\partial a}{\partial \theta} b^2 c H_c}{\delta^3} \\
& - \frac{4 a \frac{\partial a}{\partial \eta} b^2 c H_c}{\delta^3} + \frac{4 a^3 b \frac{\partial b}{\partial \theta} H_c}{\delta^3} - \frac{6 a^2 b^2 \frac{\partial b}{\partial \eta} h c}{\delta^3} - \frac{6 a \frac{\partial a}{\partial \eta} b^3 H_c}{\delta^3} + \frac{4 a^2 \frac{\partial a}{\partial \theta} b^2 H_c}{\delta^3} - \frac{a \frac{\partial H_b}{\partial \theta}}{\delta} \\
& + \frac{a^2 c \frac{\partial H_b}{\partial \theta}}{\delta^2} + \frac{a^2 b \frac{\partial H_b}{\partial \theta}}{\delta^2} + \frac{a \frac{\partial H_b}{\partial \eta}}{\delta} - \frac{a b c \frac{\partial H_b}{\partial \eta}}{\delta^2} - \frac{a^2 b \frac{\partial H_b}{\partial \eta}}{\delta^2} + \frac{a \frac{\partial d}{\partial \theta} H_b}{2 \delta d} \\
& - \frac{c \frac{\partial d}{\partial \eta} H_b}{2 \delta d} - \frac{2 \frac{\partial c}{\partial \eta} H_b}{\delta} - \frac{\frac{\partial a}{\partial \theta} H_b}{2 \delta} + \frac{\frac{\partial a}{\partial \eta} H_b}{\delta} - \frac{3 a c \frac{\partial c}{\partial \theta} H_b}{\delta^2} - \frac{4 a^2 \frac{\partial c}{\partial \theta} H_b}{\delta^2} \\
& + \frac{3 a c \frac{\partial c}{\partial \eta} H_b}{\delta^2} + \frac{7 a b \frac{\partial c}{\partial \eta} H_b}{\delta^2} - \frac{3 a \frac{\partial b}{\partial \eta} c H_b}{2 \delta^2} - \frac{2 \frac{\partial a}{\partial \eta} b c H_b}{\delta^2} + \frac{2 a \frac{\partial a}{\partial \theta} c H_b}{\delta^2} + \frac{2 a^2 \frac{\partial b}{\partial \theta} H_b}{\delta^2} \\
& - \frac{2 a^2 \frac{\partial b}{\partial \eta} H_b}{\delta^2} + \frac{5 a \frac{\partial a}{\partial \theta} b H_b}{2 \delta^2} - \frac{3 a \frac{\partial a}{\partial \eta} b H_b}{\delta^2} + \frac{4 a^2 b c \frac{\partial c}{\partial \theta} H_b}{\delta^3} + \frac{4 a^3 b \frac{\partial c}{\partial \theta} H_b}{\delta^3} - \frac{4 a^2 b c \frac{\partial c}{\partial \eta} H_b}{\delta^3} \\
& - \frac{6 a^2 b^2 \frac{\partial c}{\partial \eta} H_b}{\delta^3} - \frac{2 a^3 \frac{\partial b}{\partial \theta} c H_b}{\delta^3} + \frac{3 a^2 b \frac{\partial b}{\partial \eta} c H_b}{\delta^3} + \frac{3 a \frac{\partial a}{\partial \eta} b^2 c H_b}{\delta^3} - \frac{2 a^2 \frac{\partial a}{\partial \theta} b c H_b}{\delta^3} - \frac{2 a^3 b \frac{\partial b}{\partial \theta} H_b}{\delta^3} \\
& + \frac{2 a^3 b \frac{\partial b}{\partial \eta} H_b}{\delta^3} - \frac{2 a^2 \frac{\partial a}{\partial \theta} b^2 H_b}{\delta^3} + \frac{2 a^2 \frac{\partial a}{\partial \eta} b^2 H_b}{\delta^3} - \frac{c \frac{\partial H_a}{\partial \theta}}{\delta} - \frac{2 b \frac{\partial H_a}{\partial \theta}}{\delta} + \frac{a b c \frac{\partial H_a}{\partial \theta}}{\delta^2} \\
& + \frac{a b^2 \frac{\partial H_a}{\partial \theta}}{\delta^2} + \frac{b \frac{\partial H_a}{\partial \eta}}{\delta} - \frac{b^2 c \frac{\partial H_a}{\partial \eta}}{\delta^2} - \frac{a b^2 \frac{\partial H_a}{\partial \eta}}{\delta^2} + \frac{2 \frac{\partial c}{\partial \theta} H_a}{\delta} - \frac{3 \frac{\partial b}{\partial \theta} H_a}{2 \delta} \\
& + \frac{\frac{\partial b}{\partial \eta} H_a}{\delta} - \frac{4 b c \frac{\partial c}{\partial \theta} H_a}{\delta^2} - \frac{6 a b \frac{\partial c}{\partial \theta} H_a}{\delta^2} + \frac{3 b c \frac{\partial c}{\partial \eta} H_a}{\delta^2} + \frac{5 b^2 \frac{\partial c}{\partial \eta} H_a}{\delta^2} + \frac{2 a \frac{\partial b}{\partial \theta} c H_a}{\delta^2} \\
& - \frac{5 b \frac{\partial b}{\partial \eta} c H_a}{2 \delta^2} + \frac{2 \frac{\partial a}{\partial \theta} b c H_a}{\delta^2} + \frac{7 a b \frac{\partial b}{\partial \theta} H_a}{2 \delta^2} - \frac{3 a b \frac{\partial b}{\partial \eta} H_a}{\delta^2} + \frac{3 \frac{\partial a}{\partial \theta} b^2 H_a}{\delta^2} - \frac{2 \frac{\partial a}{\partial \eta} b^2 H_a}{\delta^2} \\
& + \frac{4 a b^2 c \frac{\partial c}{\partial \theta} H_a}{\delta^3} + \frac{4 a^2 b^2 \frac{\partial c}{\partial \theta} H_a}{\delta^3} - \frac{4 a b^2 c \frac{\partial c}{\partial \eta} H_a}{\delta^3} - \frac{6 a b^3 \frac{\partial c}{\partial \eta} H_a}{\delta^3} - \frac{2 a^2 b \frac{\partial b}{\partial \theta} c H_a}{\delta^3} + \frac{3 a b^2 \frac{\partial b}{\partial \eta} c H_a}{\delta^3} \\
& + \frac{3 \frac{\partial a}{\partial \eta} b^3 c H_a}{\delta^3} - \frac{2 a \frac{\partial a}{\partial \theta} b^2 c H_a}{\delta^3} - \frac{2 a^2 b^2 \frac{\partial b}{\partial \theta} H_a}{\delta^3} + \frac{2 a^2 b^2 \frac{\partial b}{\partial \eta} H_a}{\delta^3} - \frac{2 a \frac{\partial a}{\partial \theta} b^3 H_a}{\delta^3} + \frac{2 a \frac{\partial a}{\partial \eta} b^3 H_a}{\delta^3} \\
& - \frac{\frac{\partial H_d}{\partial \theta}}{d} + \frac{\frac{\partial d}{\partial \theta} H_d}{2 d^2}.
\end{aligned}$$

The evolution equations for the conformal three-metric components are given as follows. The metric evolution for $\hat{\gamma}_{11} = a$:

$$\frac{\partial a}{\partial t} = -2 \alpha H_a + \frac{4 a \beta^\theta}{\psi} \frac{\partial \psi}{\partial \theta} + \frac{4 a \beta^\eta}{\psi} \frac{\partial \psi}{\partial \eta} + 2 \frac{\partial \beta^\theta}{\partial \eta} c + \frac{\partial a}{\partial \theta} \beta^\theta + 2 a \frac{\partial \beta^\eta}{\partial \eta} + \frac{\partial a}{\partial \eta} \beta^\eta.$$

The metric evolution for $\hat{\gamma}_{22} = b$:

$$\frac{\partial b}{\partial t} = -2\alpha H_b + \frac{4b\beta^\theta}{\psi} \frac{\partial\psi}{\partial\theta} + \frac{4b\beta^\eta}{\psi} \frac{\partial\psi}{\partial\eta} + 2\frac{\partial\beta^\theta}{\partial\theta} c + 2b\frac{\partial\beta^\theta}{\partial\theta} + \frac{\partial b}{\partial\theta} \beta^\theta + \frac{\partial b}{\partial\eta} \beta^\eta.$$

The metric evolution for $\hat{\gamma}_{12} = c$:

$$\frac{\partial c}{\partial t} = -2\alpha H_c + \frac{4c\beta^\theta}{\psi} \frac{\partial\psi}{\partial\theta} + \frac{4c\beta^\eta}{\psi} \frac{\partial\psi}{\partial\eta} + \beta^\theta \frac{\partial c}{\partial\theta} + \beta^\eta \frac{\partial c}{\partial\eta} + \frac{\partial\beta^\theta}{\partial\theta} c + \frac{\partial\beta^\eta}{\partial\eta} c + b\frac{\partial\beta^\theta}{\partial\eta} + a\frac{\partial\beta^\eta}{\partial\theta}.$$

The metric evolution for $\hat{\gamma}_{33} = d$:

$$\frac{\partial d}{\partial t} = -2\alpha H_d + 2\beta^\theta d \cot\theta + \frac{4d\beta^\theta}{\psi} \frac{\partial\psi}{\partial\theta} + \frac{4d\beta^\eta}{\psi} \frac{\partial\psi}{\partial\eta} + \beta^\theta \frac{\partial d}{\partial\theta} + \beta^\eta \frac{\partial d}{\partial\eta}.$$

Finally the equations that govern the evolution of the extrinsic curvature components are the metric evolution for $\hat{K}_{11} = H_a$:

$$\begin{aligned} \frac{\partial H_a}{\partial t} = & \frac{4\beta^\theta H_a}{\psi} \frac{\partial\psi}{\partial\theta} + \frac{2a}{\delta} \frac{\partial\alpha}{\partial\eta} c \frac{\partial\psi}{\partial\theta} - \frac{2a^2}{\delta} \frac{\partial\alpha}{\partial\theta} \frac{\partial\psi}{\partial\theta} + \frac{4\beta^\eta H_a}{\psi} \frac{\partial\psi}{\partial\eta} + \frac{2a}{\delta} \frac{\partial\alpha}{\partial\theta} c \frac{\partial\psi}{\partial\eta} - \frac{2a}{\delta} \frac{\partial\alpha}{\partial\eta} b \frac{\partial\psi}{\partial\theta} \\ & + \frac{4}{\psi^5} \frac{\partial\alpha}{\partial\eta} \frac{\partial\psi}{\partial\eta} - \frac{\partial\alpha}{\partial\eta} c \frac{\partial c}{\partial\eta} + \frac{a}{\delta} \frac{\partial\alpha}{\partial\theta} \frac{\partial c}{\partial\eta} - \frac{\partial\alpha}{\partial\eta} \frac{\partial\alpha}{\partial\theta} c + \frac{\partial\alpha}{\partial\theta} \frac{\partial\alpha}{\partial\eta} c + \frac{\partial\alpha}{\partial\eta} \frac{\partial\alpha}{\partial\eta} b \\ & - \frac{a}{2\delta} \frac{\partial\alpha}{\partial\theta} \frac{\partial\alpha}{\partial\theta} - \frac{\partial^2\alpha}{\partial\eta^2} - \frac{2\alpha\alpha H_c^2}{\delta} + \frac{2\alpha c H_a H_c}{\delta} + 2\frac{\partial\beta^\theta}{\partial\eta} H_c + \frac{a\alpha H_a H_b}{\delta} \\ & + \beta^\theta \frac{\partial H_a}{\partial\theta} + \beta^\eta \frac{\partial H_a}{\partial\eta} - \frac{\alpha b H_a^2}{\delta} + \frac{\alpha H_d H_a}{d} + 2\frac{\partial\beta^\eta}{\partial\eta} H_a + \frac{R_{\eta\eta} \alpha}{\psi^4}. \end{aligned}$$

The metric evolution for $\hat{K}_{22} = H_b$:

$$\begin{aligned} \frac{\partial H_b}{\partial t} = & \frac{4\beta^\theta H_b}{\psi} \frac{\partial\psi}{\partial\theta} + \frac{2}{\delta} \frac{\partial\alpha}{\partial\eta} b c \frac{\partial\psi}{\partial\theta} - \frac{2a}{\delta} \frac{\partial\alpha}{\partial\theta} b \frac{\partial\psi}{\partial\theta} + \frac{4}{\psi^5} \frac{\partial\alpha}{\partial\theta} \frac{\partial\psi}{\partial\theta} + \frac{4\beta^\eta H_b}{\psi} \frac{\partial\psi}{\partial\eta} + \frac{2}{\delta} \frac{\partial\alpha}{\partial\theta} b c \frac{\partial\psi}{\partial\eta} \\ & - \frac{2}{\delta} \frac{\partial\alpha}{\partial\eta} b^2 \frac{\partial\psi}{\partial\eta} - \frac{\partial\alpha}{\partial\theta} c \frac{\partial c}{\partial\theta} + \frac{\partial\alpha}{\partial\eta} b \frac{\partial c}{\partial\theta} - \frac{\partial\alpha}{\partial\eta} \frac{\partial b}{\partial\theta} c + \frac{\partial\alpha}{\partial\theta} \frac{\partial b}{\partial\eta} c + \frac{a}{2\delta} \frac{\partial\alpha}{\partial\theta} \frac{\partial b}{\partial\theta} \\ & - \frac{\partial\alpha}{2\delta} \frac{b}{\psi^4} \frac{\partial b}{\partial\eta} - \frac{\partial^2\alpha}{\psi^4} - \frac{2\alpha b H_c^2}{\delta} + \frac{2\alpha c H_b H_c}{\delta} + 2\frac{\partial\beta^\eta}{\partial\theta} H_c \beta^\theta \frac{\partial H_b}{\partial\theta} \\ & + \beta^\eta \frac{\partial H_b}{\partial\eta} - \frac{a\alpha H_b^2}{\delta} + \frac{\alpha b H_a H_b}{\delta} + \frac{\alpha H_d H_b}{d} + 2\frac{\partial\beta^\theta}{\partial\theta} H_b + \frac{R_{\theta\theta} \alpha}{\psi^4}. \end{aligned}$$

The metric evolution for $\hat{K}_{12} = H_c$:

$$\begin{aligned} \frac{\partial H_c}{\partial t} = & \frac{4\beta^\theta H_c}{\psi} \frac{\partial\psi}{\partial\theta} - \frac{2a}{\delta} \frac{\partial\alpha}{\partial\theta} c \frac{\partial\psi}{\partial\theta} + \frac{2a}{\delta} \frac{\partial\alpha}{\partial\eta} b \frac{\partial\psi}{\partial\theta} + \frac{4\beta^\eta H_c}{\psi} \frac{\partial\psi}{\partial\eta} - \frac{2}{\delta} \frac{\partial\alpha}{\partial\eta} b c \frac{\partial\psi}{\partial\eta} + \frac{2a}{\delta} \frac{\partial\alpha}{\partial\theta} b \frac{\partial\psi}{\partial\theta} \\ & - \frac{\partial\alpha}{2\delta} \frac{\partial b}{\partial\eta} c - \frac{\partial\alpha}{2\delta} \frac{\partial\alpha}{\partial\theta} c + \frac{a}{2\delta} \frac{\partial\alpha}{\partial\theta} \frac{\partial b}{\partial\eta} + \frac{\partial\alpha}{2\delta} \frac{\partial\alpha}{\partial\theta} b - \frac{\partial^2\alpha}{\psi^4} + \beta^\theta \frac{\partial H_c}{\partial\theta} \\ & + \beta^\eta \frac{\partial H_c}{\partial\eta} - \frac{a\alpha H_b H_c}{\delta} - \frac{\alpha b H_a H_c}{\delta} + \frac{\alpha H_d H_c}{d} + \frac{\partial\beta^\theta}{\partial\theta} H_c + \frac{\partial\beta^\eta}{\partial\eta} H_c \\ & + \frac{2\alpha c H_a H_b}{\delta} + \frac{\partial\beta^\theta}{\partial\eta} H_b + \frac{\partial\beta^\eta}{\partial\theta} H_a + \frac{R_{\eta\theta} \alpha}{\psi^4}. \end{aligned}$$

The metric evolution for $\hat{K}_{33} = H_d$:

$$\begin{aligned} \frac{\partial H_d}{\partial t} = & \frac{\partial\alpha}{\partial\eta} c d \cot\theta - \frac{a}{\delta} \frac{\partial\alpha}{\partial\theta} d \cot\theta + 2\beta^\theta H_d \cot\theta + \frac{4\beta^\theta H_d}{\psi} \frac{\partial\psi}{\partial\theta} + \frac{2}{\delta} \frac{\partial\alpha}{\partial\eta} c d \frac{\partial\psi}{\partial\theta} - \frac{2a}{\delta} \frac{\partial\alpha}{\partial\theta} d \frac{\partial\psi}{\partial\theta} \\ & + \frac{4\beta^\eta H_d}{\psi} \frac{\partial\psi}{\partial\eta} + \frac{2}{\delta} \frac{\partial\alpha}{\partial\theta} c d \frac{\partial\psi}{\partial\eta} - \frac{2}{\delta} \frac{\partial\alpha}{\partial\eta} b d \frac{\partial\psi}{\partial\eta} + \frac{\partial\alpha}{2\delta} \frac{\partial c}{\partial\theta} \frac{\partial d}{\partial\theta} - \frac{a}{2\delta} \frac{\partial\alpha}{\partial\theta} \frac{\partial d}{\partial\theta} + \frac{\partial\alpha}{2\delta} \frac{c}{\psi^4} \frac{\partial d}{\partial\eta} \\ & - \frac{\partial\alpha}{2\delta} \frac{b}{\psi^4} \frac{\partial d}{\partial\eta} - \frac{2\alpha c H_d H_c}{\delta} + \frac{a\alpha H_d H_b}{\delta} + \frac{\alpha b H_d H_a}{\delta} + \beta^\theta \frac{\partial H_d}{\partial\theta} + \beta^\eta \frac{\partial H_d}{\partial\eta} - \frac{\alpha H_d^2}{d} + \frac{R_{\phi\phi} \alpha}{\psi^4 \sin^2\theta}. \end{aligned}$$

- [1] R. Vogt, in *Sixth Marcel Grossman Meeting on General Relativity Proceedings, Kyoto, Japan, 1991*, edited by H. Sato and T. Nakamura (World Scientific, Singapore, 1992), pp. 244–266.
- [2] P. Anninos, D. Hobill, E. Seidel, L. Smarr, and W.-M. Suen, Technical Report No. 11111, National Center for Supercomputing Applications.
- [3] D. Bernstein, D. Hobill, E. Seidel, and L. Smarr, *Phys. Rev. D* **50**, 3760 (1994).
- [4] A. Abrahams, D. Bernstein, D. Hobill, E. Seidel, and L. Smarr, *Phys. Rev. D* **45**, 3544 (1992).
- [5] D. Bernstein, Ph.D. thesis, University of Illinois Urbana-Champaign, 1993.
- [6] D. Bernstein and K. P. Tod, *Phys. Rev. D* **49**, 2808 (1994).
- [7] P. Anninos, D. Bernstein, D. Hobill, E. Seidel, L. Smarr, and J. Towns, in *Computational Astrophysics: Gas Dynamics and Particle Methods*, edited by W. Benz, J. Barnes, E. Muller, and M. Norman (Springer-Verlag, New York, 1994), to appear.
- [8] J. York, in *Sources of Gravitational Radiation*, edited by L. Smarr (Cambridge University Press, Cambridge, England, 1979).
- [9] R. Arnowitt, S. Deser, and C. W. Misner, in *Gravitation: An Introduction to Current Research*, edited by L. Witten (Wiley, New York, 1962).
- [10] A. Lichnerowicz, *J. Math. Pures Appl.* **23**, 37 (1944).
- [11] D. S. Brill, *Ann. Phys. (N.Y.)* **7**, 466 (1959).
- [12] C. Misner, *Phys. Rev.* **118**, 1110 (1960).
- [13] M. Choptuik, *Phys. Rev. D* **44**, 3124 (1991).
- [14] D. Bernstein, D. Hobill, and L. Smarr, in *Frontiers in Numerical Relativity*, edited by C. Evans, L. Finn, and D. Hobill (Cambridge University Press, Cambridge, England, 1989).
- [15] S. Lee, Ph.D. thesis, University of Illinois, Urbana, 1993.
- [16] S. Lee, L. Petzold, P. Saylor, and E. Seidel (in preparation).
- [17] G. Cook, Ph.D. thesis, University of North Carolina at Chapel Hill, Chapel Hill, North Carolina, 1990.
- [18] L. Smarr, in *Sources of Gravitational Radiation* [8], p. 245.
- [19] P. Anninos, D. Hobill, E. Seidel, L. Smarr, and W.-M. Suen, *Phys. Rev. Lett.* **71**, 2851 (1993).
- [20] P. Anninos, D. Bernstein, S. Brandt, D. Hobill, E. Seidel, and L. Smarr, *Phys. Rev. D* **50**, 3801 (1994).
- [21] A. Čadež, Ph.D. thesis, University of North Carolina at Chapel Hill, 1971.
- [22] L. Smarr, A. Čadež, B. DeWitt, and K. Eppley, *Phys. Rev. D* **14**, 2443 (1976).
- [23] F. Estabrook, H. Wahlquist, S. Christensen, B. DeWitt, L. Smarr, and E. Tsang, *Phys. Rev. D* **7**, 2814 (1973).
- [24] J. Wheeler, in *Relativity, Groups, and Topology (Les Houches, France, 1964)*, edited by C. DeWitt and B. DeWitt (Gordon and Breach, New York, 1964), pp. 316–520.
- [25] K. Eppley, *Phys. Rev. D* **16**, 1609 (1977).
- [26] K. Eppley, in *Sources of Gravitational Radiation* [8], p. 275.
- [27] S. M. Miyama, *Prog. Theor. Phys.* **65**, 894 (1981).
- [28] A. Abrahams and C. Evans, *Phys. Rev. D* **46**, R4117 (1992).
- [29] J. York, in *Frontiers in Numerical Relativity* [14].
- [30] C. Evans, in *Dynamical Spacetimes and Numerical Relativity*, edited by J. Centrella (Cambridge University Press, Cambridge, England, 1986).
- [31] E. Seidel and W.-M. Suen, *Phys. Rev. Lett.* **69**, 1845 (1992).
- [32] S. W. Hawking, in *Black Holes*, edited by C. DeWitt and B. S. DeWitt (Gordon and Breach, New York, 1973).
- [33] B. Reinhardt, *J. Math. Phys.* **14**, 719 (1973).
- [34] K. Eppley, Ph.D. thesis, Princeton University, 1975.
- [35] D. Eardley and L. Smarr, *Phys. Rev. D* **19**, 2239 (1979).
- [36] L. Smarr and J. York, *Phys. Rev. D* **17**, 1945 (1978).
- [37] N. Ó Murchada and J. York, *J. Math. Phys.* **14**, 1551 (1973).
- [38] W. H. Press, B. P. Flannery, S. A. Teukolsky, and W. T. Vetterling, *Numerical Recipes* (Cambridge University Press, Cambridge, England, 1986).
- [39] L. Smarr, Ph.D. thesis, University of Texas, Austin, 1975.
- [40] D. A. Anderson, J. C. Tannehill, and R. H. Fletcher, *Computational Fluid Mechanics and Heat Transfer* (Hemisphere, New York, 1984).
- [41] E. Seidel and W.-M. Suen, *Phys. Rev. D* **42**, 384 (1990).
- [42] G. Golub and C. van Loan, *Matrix Computations*, 2nd ed. (The Johns Hopkins University Press, Baltimore, Maryland, 1991).
- [43] M. R. Hestenes and E. Stiefel, *J. Res. Nat. Bur. Standards* **49**, 409 (1952).
- [44] R. Fletcher, *Lecture Notes in Mathematics 506* (Springer-Verlag, New York, 1976), pp. 73–89.
- [45] P. Sonneveld, *SIAM J. Sci. Stat. Comput.* **10**, 36 (1989).
- [46] H. van der Vorst, *SIAM J. Sci. Stat. Comput.* **13**, 631 (1992).
- [47] Y. Saad and M. H. Schultz, *SIAM J. Sci. Stat. Comput.* **7**, 856 (1986).
- [48] P. Concus and G. H. Golub, *Lecture Notes in Economics and Mathematical Systems* (Springer-Verlag, New York, 1976), Vol. 134, pp. 56–65.
- [49] S. Schaffer (private communication).
- [50] Thornburg, Ph.D. thesis, University of British Columbia, 1993.
- [51] S. Chandrasekhar, *The Mathematical Theory of Black Holes* (Oxford University Press, Oxford, England, 1983).
- [52] P. Anninos, D. Bernstein, S. Brandt, J. Libson, J. Massó, E. Seidel, L. Smarr, W.-M. Suen, and P. Walker (unpublished).